General Disclaimer

One or more of the Following Statements may affect this Document

- This document has been reproduced from the best copy furnished by the organizational source. It is being released in the interest of making available as much information as possible.

- This document may contain data, which exceeds the sheet parameters. It was furnished in this condition by the organizational source and is the best copy available.

- This document may contain tone-on-tone or color graphs, charts and/or pictures, which have been reproduced in black and white.

- This document is paginated as submitted by the original source.

- Portions of this document are not fully legible due to the historical nature of some of the material. However, it is the best reproduction available from the original submission.

UNIVERSITY OF ILLINOIS
URBANA

AERONOMY REPORT NO. 107

FEED SYSTEM DESIGN AND EXPERIMENTAL RESULTS IN THE UHF MODEL STUDY FOR THE PROPOSED URBANA PHASED ARRAY

by
J. T. Loane
S. A. Bowhill
P. E. Mayes

December 1, 1982

Library of Congress ISSN 0568-0581

Aeronomy Laboratory
Department of Electrical Engineering
University of Illinois
Urbana, Illinois

Supported by
National Aeronautics and Space Administration

UILU-ENG-82 2507

A E R O N O M Y R E P O R T

N O. 107

FEED SYSTEM DESIGN AND EXPERIMENTAL RESULTS IN THE UHF MODEL STUDY FOR THE PROPOSED URBANA PHASED ARRAY

by
J. T. Loane
S. A. Bowhill
P. E. Mayes

December 1, 1982

Supported by
National Science Foundation
Grants ATM 80-02049 and 81-20371

Aeronomy Laboratory
Department of Electrical Engineering
University of Illinois
Urbana, Illinois

ABSTRACT

The observable effects of atmospheric turbulence and the basis for the coherent-scatter radar technique are discussed. The reasons are given for upgrading the present Urbana Radar system to a larger steerable array. Phased-array theory pertinent to the system design is reviewed, along with approximations for maximum directive gain and blind angles due to mutual coupling.

The methods and construction techniques employed in the UHF model study are explained. The antenna range is described, with a block diagram for the mode of operation used. The resulting plots are shown, and agreement and disagreement with theory is discussed. Suggestions for a feasible full-scale switching network are given for a proposed 25 acre array.

TABLE OF CONTENTS

LIST OF TABLES

LIST OF FIGURES

Figure — Page

1. INTRODUCTION

1.1 Incoherent or Thomson Scatter

Ever since the 1950s, radar investigations of scattered power returns from the ionosphere have been feasible with high-powered HF and VHF equipment, and since the early 1960s several nations have conducted such studies from radar facilities throughout the world. It is known that the echo power from a volume of air with radar cross section σ is proportional to the mean square deviation of the permittivity

$$\overline{\left|\frac{\Delta\epsilon}{\epsilon}\right|^2} = \frac{1}{v}\int \left|\frac{\Delta\epsilon}{\epsilon}\right|^2 dv \quad (\propto \sigma)$$

over the scattering volume v. Evans (1969) has reviewed the development of the method known as Thomson scatter used to obtain electron-density profiles, electron and ion kinetic temperatures, and other practically deduced information available from ground-based radar. Thermal fluctuations of ions have been seen to produce backscatter of randomly distributed phase with respect to the incoming signal, giving rise to the alternative term incoherent scatter. For an exploring wavelength much larger than the electron Debye length (Buneman, 1962; Farley et al., 1961) the radar cross section per unit volume has been shown to be approximately

$$\sigma = \frac{\sigma_e N_e}{1 + T_e/T_i}$$

where N_e is the electron number density, σ_e is the radar cross section of a single electron, and T_e/T_i is the ratio of electron and ion temperatures, which has always been observed to be in the range from 1 to 4. Data are frequently calibrated by rocket, ionosonde, and other types of experimentation (sometimes T_e and T_i must be assumed in order to determine N_e, or vice

versa; the neutral kinetic temperature and the neutral density may be deduced from T_e and T_i). Doppler shifting broadens the scattered spectrum of a monochromatic probing signal by the amount

$$\Delta f_e = \frac{1}{\lambda}\sqrt{\frac{8kT_e}{m_e}} \quad \text{(3 dB bandwidth)}$$

where $k = 1.380 \times 10^{-23}$ JK^{-1} = Boltzmann's constant and $m_e = 9.109 \times 10^{-31}$ kg is the mass of an electron. A similar expression describes the ionic spectral component Δf_i. The longer-wavelength case (VHF) in which the largest amount of scattered power is seen to be in the double-humped spectrum of width Δf_i has historically been of greater interest (Allman and Bowhill, 1976). One reason is that the bandwidth Δf_e may be one or two orders of magnitude greater than Δf_i and sufficiently sensitive equipment over such a broad band was nonexistent in the early 1960s. A great deal has nevertheless been learned about ion-neutral and ion-ion collisions, ionic composition, electric currents, magnetic fields, the velocity distribution of photoelectrons, and plasma drift velocities from Thomson-scatter measurement.

1.2 Coherent Scatter and the Urbana Radar

In the mid-1960s, investigations of the D region (below 90 km altitude) by UHF from the Arecibo, Puerto Rico facility and by VHF radar from Jicamarca, Peru revealed echoes returning more power than that predicted by Thomson scatter alone. Rastogi and Woodman (1974) working at Jicamarca showed that the mean echo power was 4 dB above what was expected due to thermal motions of electrons. Minute-by-minute fluctuations in measured wind velocities and echo power suggested a nonthermal mechanism and indicated the turbulent nature of the D region. Oscillations in the vertical wind velocities are now believed to be caused by gravity waves, and the large variations in echo power (as much as 20 dB per minute) have been con-

firmed to be directly related to the rate of energy dissipation per unit mass due to neutral atmosphere turbulence. Irregular structures in the permittivity distribution make it possible to receive coherent Doppler backscatter containing line-of-sight velocity information, and "coherent-scatter" radar has become an important tool for research into the dynamics of the D region. The method seems to favor operation at lower frequencies due to a larger predetection signal-to-noise ratio (SNR) at HF and VHF than that found at UHF and above (Röttger, 1981).

A VHF coherent-scatter radar has been operating at the Aeronomy Field Station outside of Urbana, Illinois since the spring of 1978 (Gibbs and Bowhill, 1979) using a 121 m x 91 m aperture antenna array for both transmitting and receiving and a 40.92 MHz pulse transmitter (20 μs pulse width, 400 Hz repetition rate) broadcasting up to 1 MW during the duty cycle. Scattered power returns over Urbana are observed to vary considerably as a function of both altitude and time, but prominent scattering layers or peaks of high radar cross section are a consistent occurrence. Figure 1.1 shows an echo return about 10 dB above the reference level from a layer at 72 km altitude lasting longer than an hour and also a more transient peak at 81 km producing reflections up to 25 dB above the background. Some small but significant vertical shifts in these layers are also observed, usually 2 km or less but taking place sometimes within a minute. This phenomenon may be due to either tidal or gravity-wave oscillations or to the (approximately) vertical component of shear motions along the radar beam (Edwards, 1981). Figure 1.2, also from Edwards, contains line-of-sight velocity information for the same time period as Figure 1.1. Abrupt changes in phase of these oscillations as a function of altitude correspond to minima in the turbulence-induced scatter of Figure 1.1. The scattering peak at 81 km on Figure 1.1

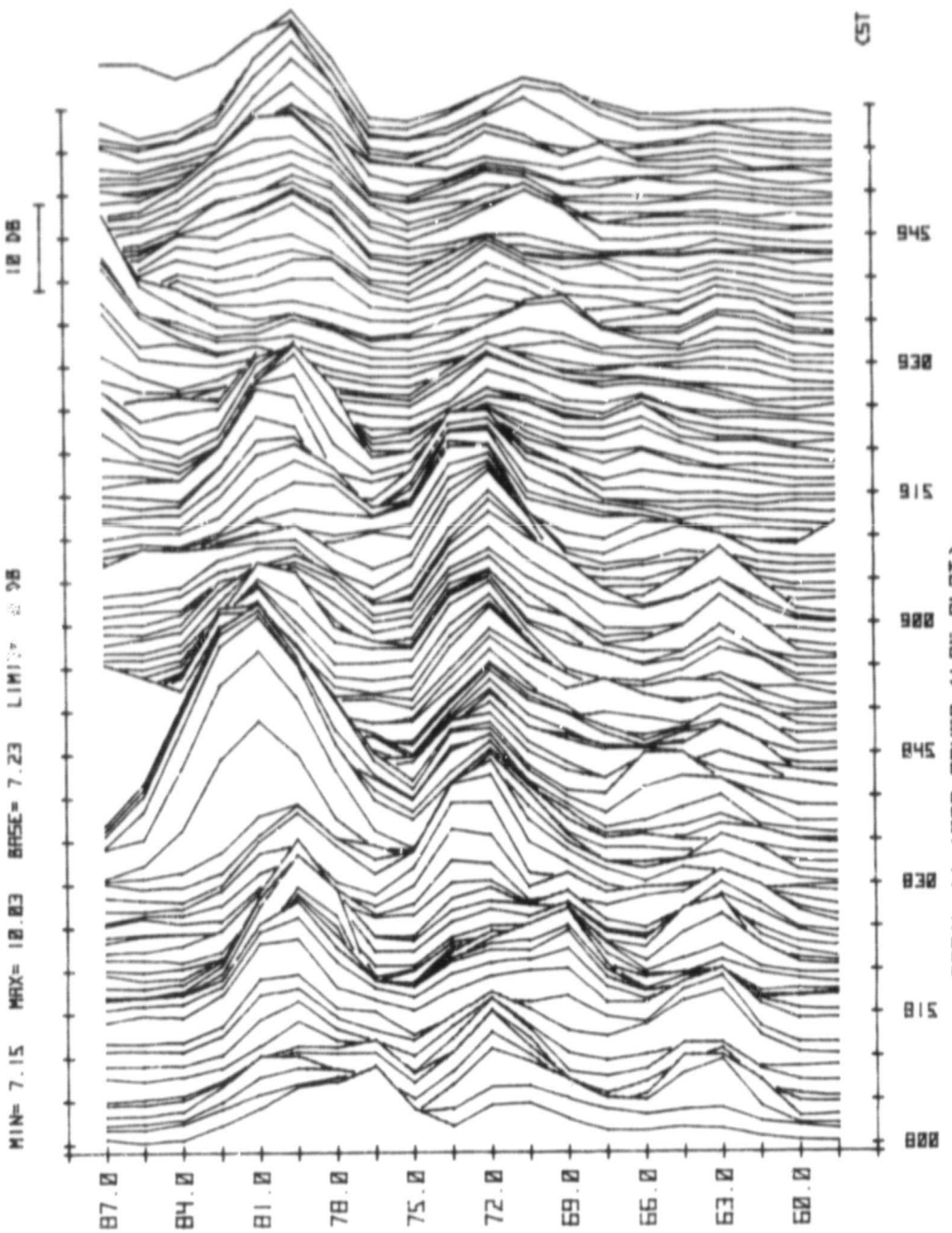

Figure 1.1 Minute-by-minute scattered power profiles between 800 and 1000 CST on April 11, 1978.

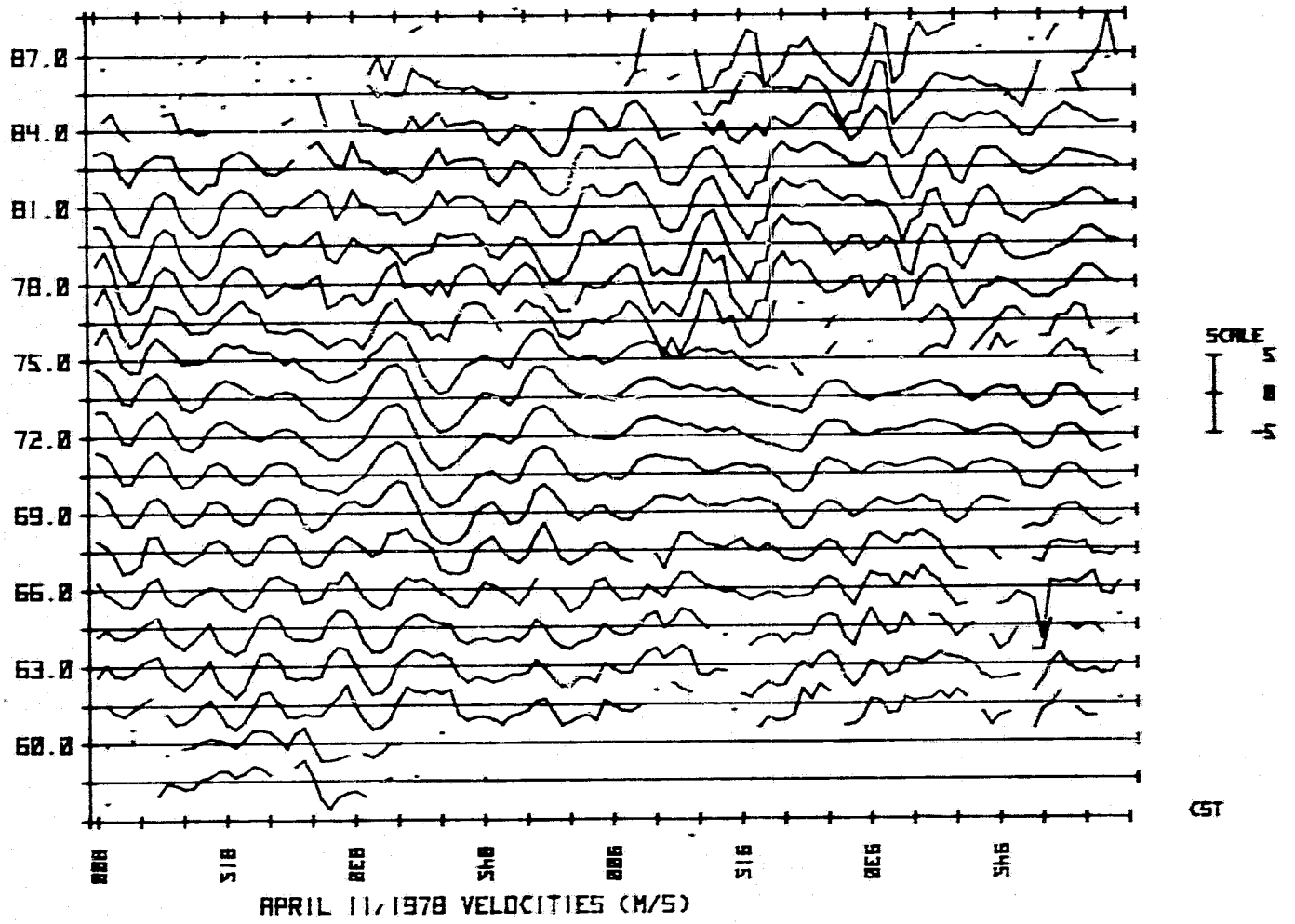

Figure 1.2 Minute-by-minute line-of-sight velocity between 800 and 1000 CST on April 11, 1978.

is interpreted as additional turbulence created by the breakup of short-period gravity waves into nonperiodic motions lasting from about 8:20 to 8:45 CST.

Hourly mean horizontal velocities for winds toward the southeast are shown in Figure 1.3 for the same time period. These velocites are calculated approximately knowing that horizontal components are usually an order of magnitude above the vertical, and since the radar beam is not exactly vertical but rather tilted about 1.5° toward S-E, the horizontal wind velocity is taken to be about 40 times the mean line-of-sight measurement. The resolution of the system is 3 km, and standard deviations from the hourly mean are also given. Peaks in the power profile of Figure 1.1 correspond to altitudes of local maxima in the mean horizontal wind velocty. But according to O. Røyrvik in Edwards (1981), it is premature to draw conclusions about the wind shear and scattered power because nothing can be known about the N-E component of velocity, and better altitude resolution is needed to investigate the relationship between the fine structure of the velocity and power profiles. Research is presently under way toward a more thorough understanding of gravity-wave, turbulence (shear), and tidal interactions.

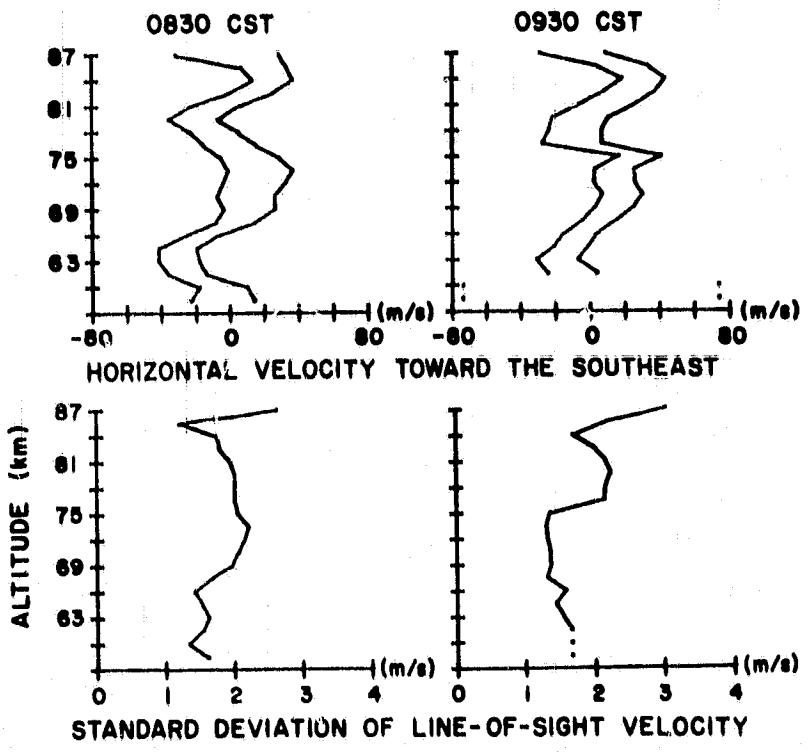

Figure 1.3 Calculated hourly means of the horizontal velocity and the standard deviation of the line-of-sight velocity profiles between 800 and 1000 CST on April 11, 1978. The two curves in the horizontal velocity profile represent the standard deviation profiles.

2. RESEARCH ON A NEW URBANA RADAR ANTENNA

2.1 Existing Proposal

Design studies have been initiated at the University of Illinois at Urbana on an upgraded antenna in the Urbana Radar system. The most cost-efficient design involves a single increased-aperture phased array with discrete-direction scanning capability. A beam steerable away from the zenith in two orthogonal planes would provide far more information about wind motion in any horizontal direction. At times the power return from certain altitudes is too weak for the present system to detect, but the proposed ninefold increase in aperture area will make it possible to receive backscatter at all times throughout the mesosphere; or a tradeoff for achieving better height resolution would be possible since the pulse width of the transmitter could be reduced by the same amount as the aperture was increased. Detailed studies could then be made of the turbulence layers responsible for coherent scatter, which are believed to be only tens to hundreds of meters thick (Rastogi and Bowhill, 1976).

The preliminary draft of the new antenna design by Mayes and Tanner (1981) was based upon the following specifications:

Aperture. The proposed antenna will have a physical aperture of $10^5 m^2$.

Operating frequency. The antenna will perform without substantial degradation over a 1.0 MHz bandwidth centered at 40.92 MHz.

Polarization. The horizontal E-vector component of the beam far from the antenna will always lie in the east-west direction. A north-south polarization will be an add-on option.

Scanning direction. The beam will be steerable in three discrete directions without loss of gain: The vertical, and 30° from vertical in the east-west and north-south vertical planes. Scanning directions 2° from the

vertical in both planes will be add-on options.

Speed of steering. The antenna will be electrically steerable from one direction to another in 1 ms or less.

Power handling capability. The antenna system will be able to handle a peak power of 6 MW with a reflection coefficient of better than -10 dB across the band.

Environmental conditions. The antenna will be able to withstand 1 inch of ice on the elements and 60 mph winds without major damage.

Some of the above requirements have since been relaxed due to prohibitive expense. An 88 x 88 element array of parallel half-wave dipoles has been agreed upon, to be erected above a grid of steel wires on the ground for better conduction. A major part of the feed system design consists of open-wire transmission lines normal to the dipoles. Unless these lines are shielded, an awkward proposition creating much additional cost, the add-on optional polarization would result in a major coupling problem destroying the simplicity of the network, and the idea has subsequently been set aside. The operation of the proposed feed system is based upon the transforming properties of uniform lossless transmission line, discussed at length in later chapters. At the extremes of the $\pm 1.22\%$ bandwidth needed for Doppler measurements, array dimensions will vary with respect to λ, and although loss or performance can be expected away from the center frequency, the only affordable procedure is to assume a monochomatic system. The present Urbana Radar antenna tolerates the same bandwidth during reception.

Another consideration is that the gain or directivity of a dipole array must necessarily vary 2 or 3 dB over the scanning directions mentioned (refer to Section 3.2), although a usable high-gain beam can still be maintained. Also since mutual effects will cause the input impedance of the

antenna ports to vary substantially over the various scanning modes, different matching networks are required for each mode, and the most feasible switching method will probably be by mechanical means taking longer than 1 ms. But one may assume that the wind velocity stays constant over the short time needed to switch between modes (and over the different scattering volumes seen by a single antenna).

The 7744 element square array under consideration has elements located on all intersection points of a grid with interelement spacing exactly $\lambda/2$ (= 12.02 feet), mounted $\lambda/4$ above ground on 4 x 4 inch square wooden posts. The dipoles will lie along one of the grid directions, each cut from 2 inch O.D. aluminum pipe with total length slightly less than $\lambda/2$ so that the ends almost touch. This configuration will provide optimum performance without making the construction requirements too critical (Mayes and Tanner, 1981). Construction details will be similar to those of the present array as recorded in Allman and Bowhill (1976). A progressive phase shift imposed upon the element current distribution will produce a scanned beam away from the vertical as discussed in Section 3.1. In addition to beams in the east-west and north-south "principal" planes, the same phase shifting network may possibly be used for scanning 45° from the vertical in corner-to-corner planes of the array.

2.2 Objectives of the Model Study

Some of the aspects of large array behavior are very expensive if not impossible to calculate or predict. The current distribution across the array dictates the shape of the beam (Chapter 3), and in practice the currents are never ideal. Errors in their distribution arise due to imperfections (losses, inexact lengths, nonuniformities, etc.) in the feed network, scattered fields from element reflections, and the difficult-to-predict

mutual coupling between excited elements. Mutual coupling is a very important consideration in large arrays which is discussed in detail in later chapters and in the references Agrawal and Lo (1972) and Lechtreck (1968). But modeling and testing a scaled-down section of the proposed array should give some indication of the problems associated with constructing a larger system. Since the receiving and transmitting properties of an antenna are identical, all testing has been done in a transmitting mode.

A 6 inch wavelength (scale ≈ 1/48) was adopted because it would be easy to work with using standard microwave techniques and would still be within the frequency range capabilities of equipment in the Electrical Engineering Department. An 8 x 8 element array was planned for testing on the rooftop UHF range, that size deemed sufficiently large to exhibit mutual coupling effects. Commercial phase shifters were available in the Department to realize the 90° shift from one element to the next necessary to displace the beam from the array normal (vertical axis). The ideal current distribution for the various beam directions are independent of the type or orientation of elements used, and the phase progression required for scanning in a principal plane and in a diagonal plane is shown in Figure 2.1 for currents of equal magnitude and $\lambda/2$ spacing. We may predict the most severe mutual coupling to occur when individual elements receive maximum radiated power from other elements, which in the case of thin dipoles is the side-by-side orientation. Defining collinear elements as being in a row, then edge rows in an array are seen to receive the most destructive mutual effects, i.e. to receive radiation the most different in the array than the more numerous central rows. Inferences concerning mutual coupling will probably be the most important outcome of testing the model array.

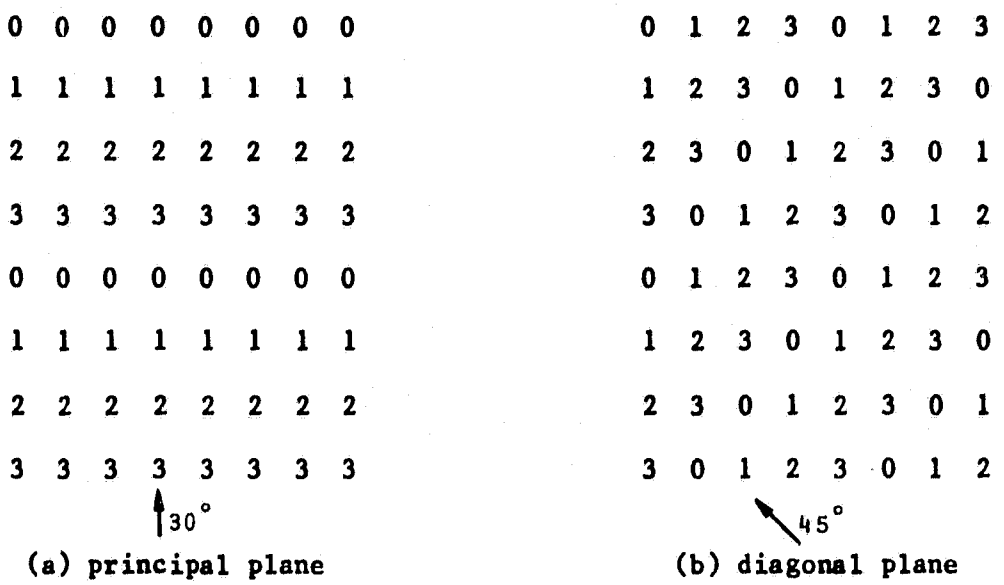

Figure 2.1 Method of element phasing to produce a beam in the direction shown. Grid numbers are multiples of 90° referring to relative phases of equal-magnitude currents. Beam angles refer to displacement from the array normal.

3. ANTENNA ARRAY THEORY

3.1 Far-Field Pattern Analysis

The total radiated field of an antenna array can be found by adding all of the individual field contributions at the point of interest. If the field far from the antenna is to be considered, then many practical arrays lend themselves readily to mathematical analysis. The linear array, shown in Figure 3.1, is an arrangement of elements equally spaced d_x units apart along the x-axis. In the far-field region, usually chosen to be at least a distance $r=2D^2/\lambda$ from the array where D is the largest array dimension, the 1/r dependence is ignored between elements and all rays to the observer are essentially parallel. If the phasor value of the mth individual field at the observation point is E_m , then the total field from M elements arranged in numerical order along the positive x-direction is given by

$$E = \sum_{m=1}^{M} E_m e^{jm\beta d_x \cos\theta_x}$$

where $\beta=2\pi/\lambda$ and the exponent accounts for the additional phase information seen by the observer. In a uniform array, all the source currents are of equal magnitude and the radiators are given a progressive phase shift so that the individual fields can be written as

$$E_m = E_o e^{jm\delta_x}$$

All fields now have equal strength and δ_x is the amount by which E_m leads E_{m-1}. Letting

$$\psi_x = \delta_x + \beta d_x \cos\theta_x$$

and considering the variation of the total field strength as a function of

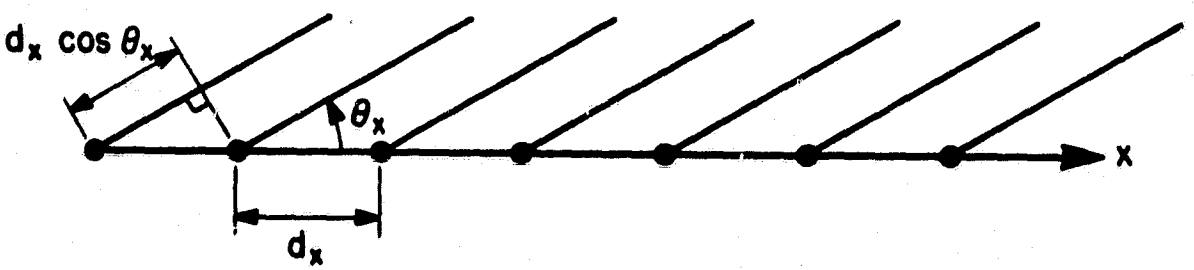

Figure 3.1 Linear antenna array with angle θ_x from the axis to the observed rays.

direction, one can obtain

$$E = E_o \sum_{m=1}^{M} e^{jm\psi_x} = E_o e^{j\psi_x} \frac{1 - e^{jM\psi_x}}{1 - e^{j\psi_x}}$$

$$= E_o e^{j(M + 1)\psi_x/2} \left[\frac{\sin(M\psi_x/2)}{\sin(\psi_x/2)} \right] \qquad (3.1)$$

The expression in brackets reaches a maximum value of M occurring at $\psi_x = 0$, and it is seen to modify the field pattern E_o of a single radiator.

Equation 3.1 holds for a uniform linear array of any type of repeated element radiating any possible E_o. Each individual radiator can itself be an array as long as the uniformity criterion is adhered to. Thus the pattern analysis can be built up for 2- and 3-dimensional uniform arrays by multiplying a series of pattern functions as follows. Since a normalized pattern at constant r is of major importance in the study of antennas, the bracketed term in Equation 3.1 is usually divided by M and written as

$$S_x = \frac{\sin(M\psi_x/2)}{M\sin(\psi_x/2)}$$

Thus the pattern function S_x peaks at unit magnitude when $\psi_x = 0$, and if the elements radiate isotropically the radiation will be directed outward along the main beam angle or scan angle θ_{xo} given by

$$\cos\theta_{xo} = \frac{-\delta_x}{\beta d_x}$$

A plot of $|S_x|$ versus ψ_x for M = 28 is given in Figure 3.2 (Allman and Bowhill, 1976). If E_o is isotropic then the pattern function of the linear array in space would be symmetrical about the x-axis. However, if this whole array is expanded uniformly along another axis (y) to make N columns of M elements, with separation d_y and possibly a progressive phase shift δ_y, then the total pattern can be computed as

$$F = f S_x S_y$$

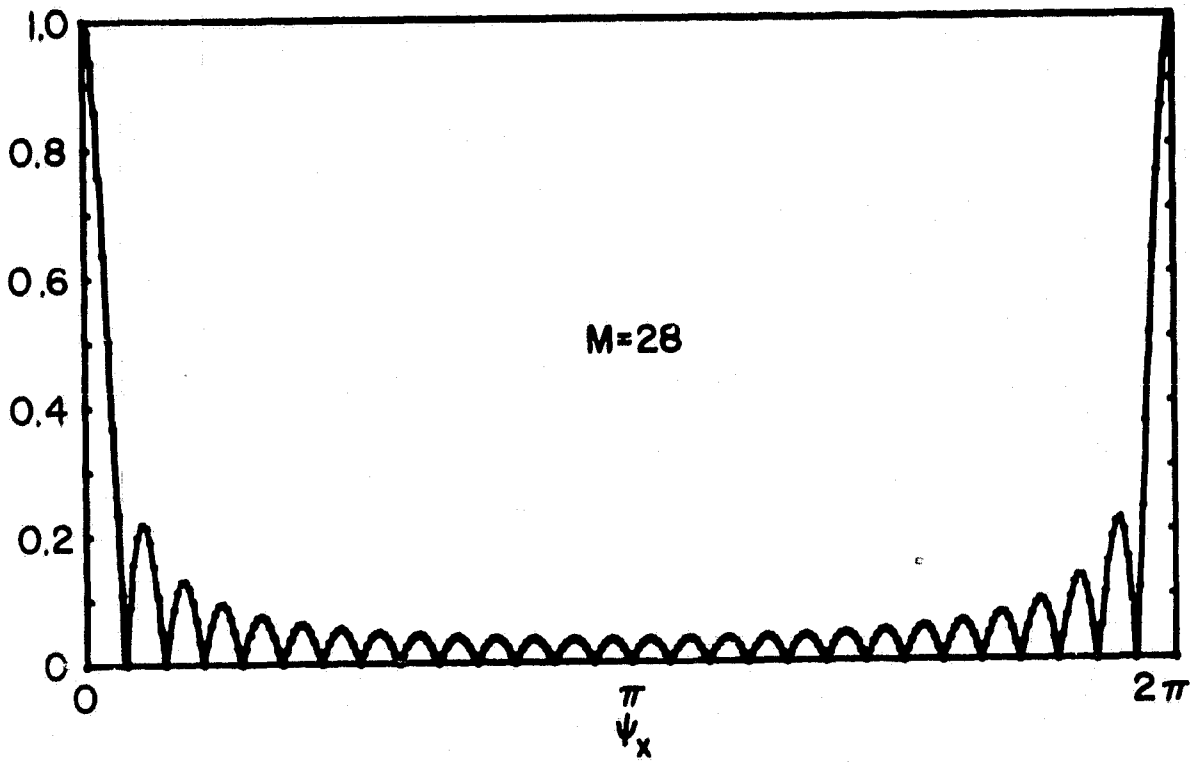

Figure 3.2 Far-field pattern $|S_x|$ for a linear array (repeats periodically).

where $$S_y = \frac{\sin(N\psi_y/2)}{N\sin(\psi_y/2)}$$

$$\psi_y = \delta_y + \beta d_y \cos\theta_y$$

and f is the normalized pattern proportional to E_o. A sketch of the coordinate system used is provided in Figure 3.3. Such arrays are designed to project a concentrated beam in the direction described by the two angles θ_{xo} and θ_{yo} ($\psi_y = 0$). No phase shift produces a "broadside" beam in the z-direction. When either $\delta_x = 0$ or $\delta_y = 0$ the array is said to be scanned in a principal plane. For f isotropic in this plane there are sidelobes in the pattern theoretically having the same magnitude as the secondary maxima of S_y or S_x respectively (see Figure 3.2), which approaches $2/3\pi = 0.2122$ as the number of elements increases. The visible range of ψ_x is from $\delta_x - \beta d_x$ to $\delta_x + \beta d_x$, similarly for ψ_y. When a planar array is mounted $d_z/2$ units above a perfectly conducting ground plane, the images below it can be considered as another array out of phase with the first by 180°. Then the pattern F would be further modified by

$$S_z = \frac{\sin\psi_z}{2\sin(\psi_z/2)}$$

$$\psi_z = \pi + \beta d_z \cos\theta_z$$

where θ_z is the direction from the z-axis to the observed ray. The final pattern function is

$$F = fS_xS_yS_z \qquad \text{(above ground plane; F = 0 below)}$$

As relevant to this study, the element pattern f or E_o is that of a half-wave thin dipole oriented in the y-direction whose current distribution for the ideal (infinitely thin) case is

$$I(y) = I(0)\cos\beta y, \quad -\lambda/4 \le y \le \lambda/4$$

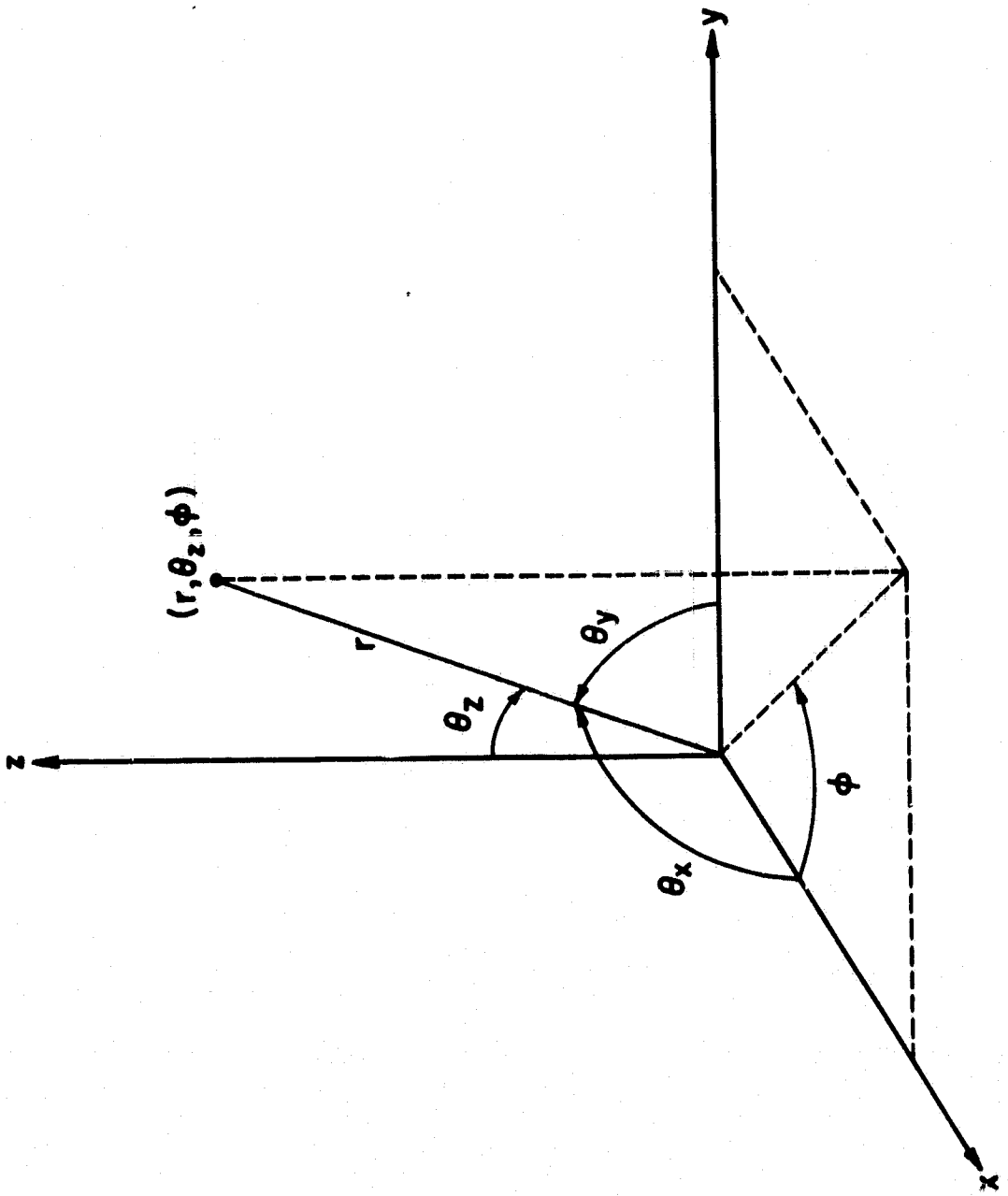

Figure 3.3 Coordinate system.

with the driving point centered at y = 0. This is a good approximation of the source currents for actual dipoles, a simplifying assumption being that secondary scattering from the elements has but a minor effect on the pattern. Ignoring secondary surface currents (on the $\lambda/4$ nonresonant excited lengths), I(y) produces the far field

$$E_o = j60I(0)\,\frac{e^{-j\beta r}}{r}\,\frac{\cos[(\pi/2)\cos\theta_y]}{\sin\theta_y}$$

This propagates as a transverse electromagnetic (TEM) wave, linearly polarized with the E vector in the same plane as the y-axis and in the direction of increasing θ_y. The factor

$$f = \frac{\cos[(\pi/2)\cos\theta_y]}{\sin\theta_y}$$

is retained as the normalized element pattern.

The dipole pattern and S_z do not have a drastic effect on the total pattern unless the beam is scanned near horizontal (the xy-plane), and f and S_z near the vertical are seen to be much more slowly varying than S_x, S_y for sufficiently large M,N. Polar plots showing these variations were made by Allman (1976) for the design of the present 24 x 36 element Urbana Radar array and are reproduced in Figure 3.4. The total pattern $|F|$ of a broadside beam has been computed as θ_y varies in the principal plane $\theta_{xo} = 90°$ for $d_y = 0.458\lambda$, $d_z = \lambda/2$, N = 36. For the model and the proposed full-scale array, computation of F has produced the values in Table 3.1 for pertinent main-beam, half-power beamwidth, and sidelobe parameters for N = M = 8 (model) and N = M = 88 (full-scale), $d_x = d_y = d_z = \lambda/2$ (a convenient spacing for construction and scanning requirements). In addition to broadside capability, the new design incorporates phase shifts of -90° for either δ_x or δ_y or both simultaneously, implying a beam essentially $\theta_{zo} = 30°$ from the

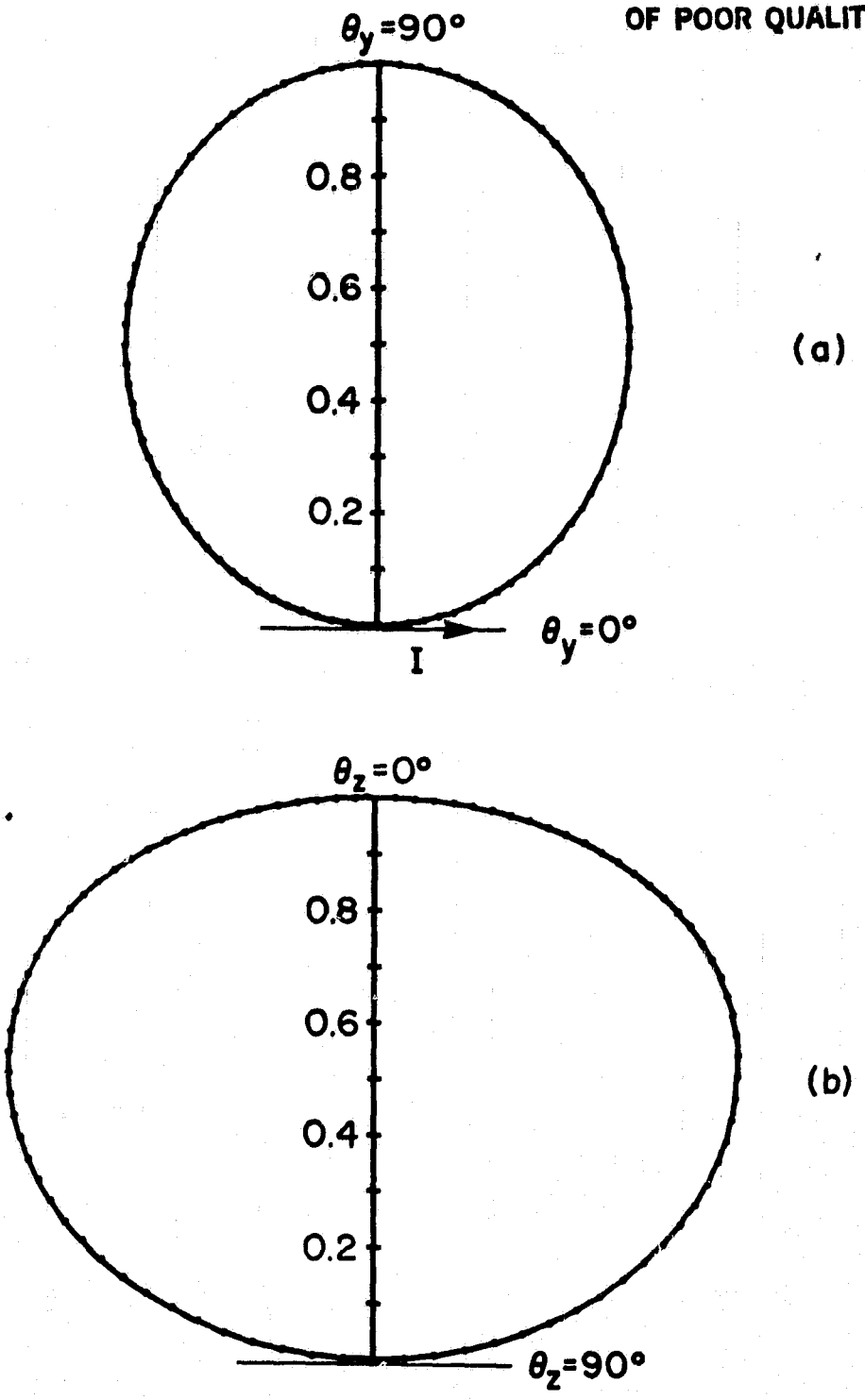

Figure 3.4 E-plane patterns for Urbana Radar array as functions of θ_y (S_x = 1).

(a) half-wave dipole f, polar

(b) image S_z, polar

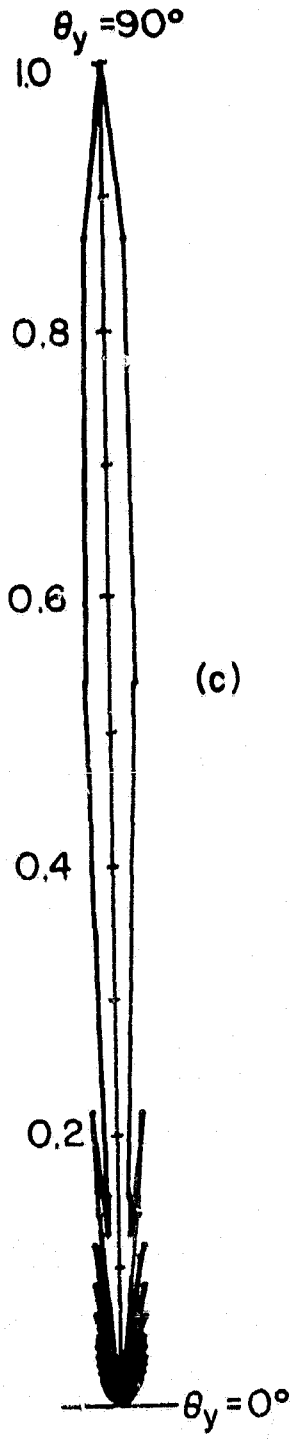

Figure 3.4 (c) total $|F|$, polar

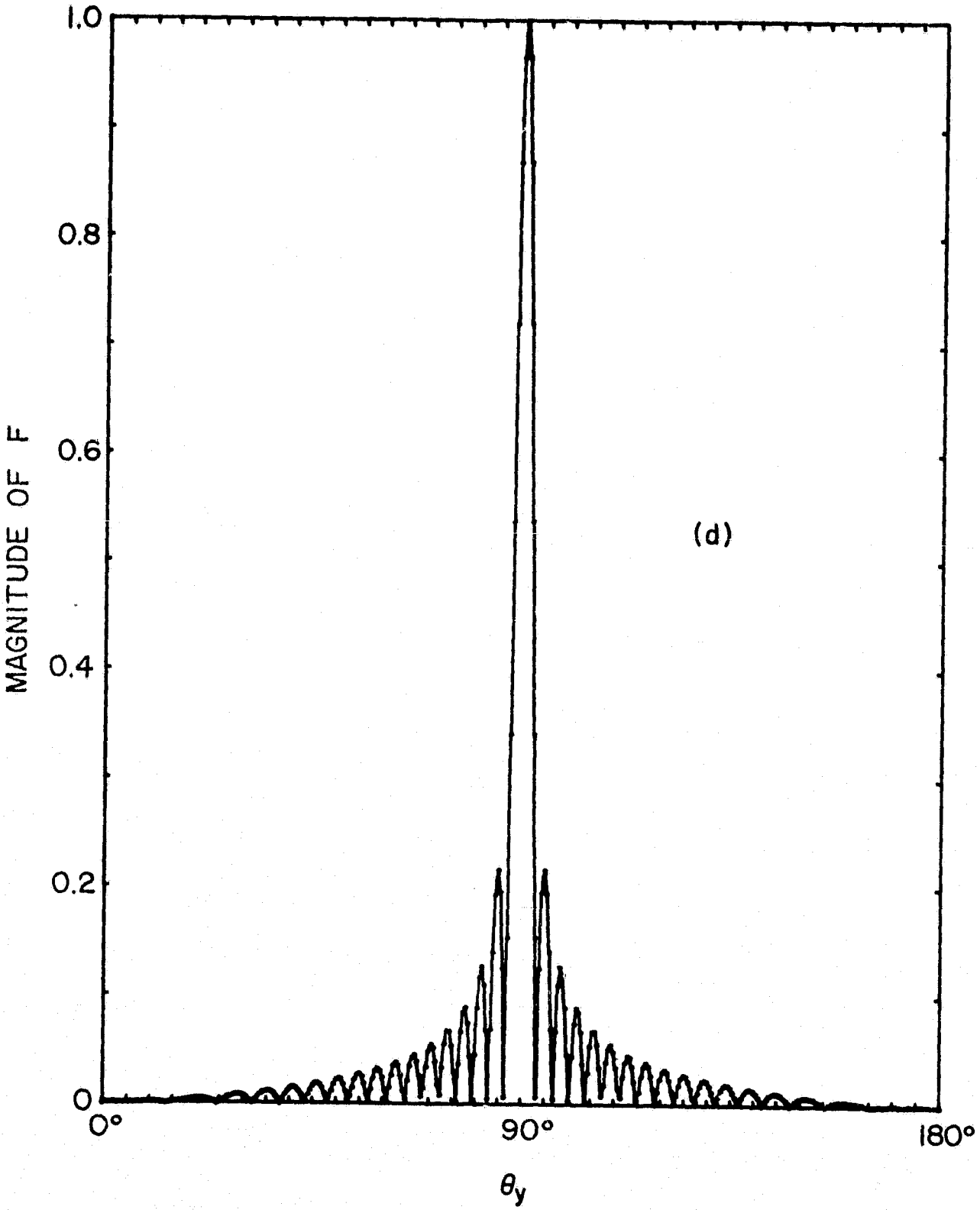

Figure 3.4 (d) total |F|, rectangular

Table 3.1 Evaluation of F. Beamwidth is defined as the difference between half-power angles. Elevation is the vertical plane containing the main-beam maximum. Sidelobes having negative θ_z are on the far side of the z-axis from the main beam. Sidelobe levels shown refer to field strength relative to the main-beam maximum.

			full-scale		model	
broadside (symmetric)	main beam angle		$\theta_{zo} = 0°$		$\theta_{zo} = 0°$	
	half-power angles		$\theta_{zH} = \pm 0.577°$	$\theta_{zE} = \pm 0.577°$	$\theta_{zH} = \pm 6.4°$	$\theta_{zE} = \pm 6.3°$
	largest sidelobes in principal-plane patterns		$\theta_{zH} = \pm 1.86°$ 0.2173	$\theta_{zE} = \pm 1.85°$ 0.2172	$\theta_{zH} = \pm 21.0°$ 0.2279	$\theta_{zE} = \pm 20.8°$ 0.2066
scanned in H-plane	main beam angle		$\theta_{zo} = 29.998°$		$\theta_{zo} = 29.7°$	
	half-power angles	in H-plane	$\theta_z = 29.334°$	$\theta_z = 30.667°$	$\theta_z = 22.7°$	$\theta_z = 37.4°$
		normal to H-plane	$\nu = -0.577°$	$\nu = 0.577°$	$\nu = -6.3°$	$\nu = 6.3°$
	largest sidelobes in elevation pattern		$\theta_z = 27.87°$ 0.2185	$\theta_z = 32.17°$ 0.2154	$\theta_z = 8.1°$ 0.2339	$\theta_z = 6.8°$ 0.1509
scanned in E-plane	main beam angle		$\theta_{zo} = 29.989°$		$\theta_{zo} = 28.8°$	
	half-power angles	in E-plane	$\theta_z = 29.327°$	$\theta_z = 30.658°$	$\theta_z = 22.0°$	$\theta_z = 36.1°$
		normal to E-plane	$\nu = -0.577°$	$\nu = 0.577°$	$\nu = -6.4°$	$\nu = 6.4°$
	largest sidelobes in elevation pattern		$\theta_z = 27.87°$ 0.2247	$\theta_z = 32.17°$ 0.2107	$\theta_z = 8.1°$ 0.2836	$\theta_z = 6.7°$ 0.1493

Table 3.1 (contd)

			full-scale		model	
scanned in diagonal plane	main beam angle		θ_{zo} = 44.982°	ϕ_o = 44.991°	θ_{zo} = 43.1°	ϕ_o = 43.9°
	half-power angles	in elevation plane	θ_z = 44.175°	θ_z = 45.837°	θ_z = 35.1°	θ_z = 52.3°
		normal to elevation plane and azimuthal	ν = -0.587° ϕ = 44.160°	ν = 0.587° ϕ = 45.822°	ν = -6.2° ϕ = 34.9°	ν = 6.7° ϕ = 53.5°
	largest sidelobes in elevation pattern		θ_z = 41.38° 0.05072	θ_z = 48.85° 0.04449	θ_z = 11.5° 0.05170	θ_z = -9.6° 0.02253

vertical in either principal plane or $\theta_{zo} = 45°$ in a "diagonal" plane containing the z-axis and the line $\phi = 45°$ ($\theta_x = \theta_y$). The deviations caused by f and S_z are very small. The yz-plane is designated as the E-plane, the xz-plane as the H-plane, and E or H subscripted angles lie in these planes. The main beam descriptors have subscript 0. Angle ν refers to displacement in the plane normal to the vertical (elevation) plane, with vertex at the origin.

Patterns evaluated in the vertical plane parallel to the excitation phase fronts will exhibit a linear broadside S_x shape exactly, and patterns evaluated over ν in that plane tilted through the beam (not near the horizon) will appear almost identical to S_x, since there is only a very small deviation from the scan angle as the observer moves normal to the elevation plane. For diagonal phase fronts a rotation of axes x,y into X,Y is appropriate to show this because if phase progression is defined in the positive X-direction, for θ_Y near 90°, θ_X and θ_z are stationary in the θ_Y direction. The exact relation is

$$\frac{\cos\theta_X}{\sin\theta_Y} = \cos\theta_{Xo} = \sin\theta_{zo} \quad (=\text{constant})$$

in the "ν-" plane normal to the elevation. For a θ_Y change of 2° with $\theta_{Xo} = 45°$, the θ_X deviation from θ_{Xo} is only 0.035°. When the phase fronts propagate diagonally, sidelobes are smaller and the beam is wider in the elevation plane since Equation 3.1, which is a Fourier transform of M impulses, approaches the (continuous array) transform of the form $(\sin^2 x)/x^2$ for a triangular pulse instead of a square pulse. Larger sidelobes are not seen in the E- and H-planes because either $\theta_x = 90°$ or $\theta_y = 90°$ which is far from $\theta_{xo} = \theta_{yo} = 60°$ (ignoring small deviations). In any scanning mode, the four largest sidelobes appear about the cone $\theta_x = \theta_{xo}$ wherever θ_y is in a

sidelobe of S_y and vice versa. In the 88 x 88 array they radiate all total about 0.2173^2 (≅ -13dB) as much power as the main beam.

3.2 Directive Gain Calculations

The intensity Φ of an an antenna is a function of direction expressing the amount of power radiated per unit solid angle towards an observer in that direction. The total power radiated is the integral of the intensity over all possible angles, or

$$P = \int \Phi \, d\Omega$$

where $d\Omega = \sin\theta_z d\theta_z \, d\phi$, and the average power radiated per steradian or the average intensity is simply $P/4\pi$. The directive gain of an antenna is the ratio of the intensity in a certain direction to that average, namely

$$g = \frac{4\pi\Phi}{P}$$

Since we are concerned with TEM radiation in the far field, then

$$g = \frac{4\pi|F^2|}{\int|F^2| \, d\Omega}$$

When the scanning characteristics are considered, one usually wants to know the maximum directive gain or directivity of the main beam

$$g_o = \frac{4\pi|F_o{}^2|}{\int|F^2| \, d\Omega} \qquad (3.2)$$

where F_o is the pattern maximum. For high-gain antennas like a phased array over most of the range of integration F^2 contributes very little to the total (see Figure 3.4d), and good approximations can be obtained by assuming that all power is radiated in the main beam at constant intensity within the half-power locus of F. For the large array broadside operation this amounts to a very nearly circular cone from the origin out to $\theta_z = 0.577°$. Actually the circle is slightly deformed, since the diagonal $\theta_z = 0.587°$. Using the

less optimistic latter value and the small angle approximation, Equation 3.2 reduces to

$$g_o = \frac{4\pi}{2\pi\int \theta_z d\theta_z} = \frac{4}{\theta_z^2} \quad (= 45.8 \text{ dB})$$

Similarly, for scanning modes it would seem reasonable to utilize an elliptical cone approximation since it is known from the pattern function that the beam should be wider in the θ_z direction than the normal. If the total beamwidth is 2τ in the vertical direction and 2ν in the horizontal, then the directivity would be close to

$$g_o \approx \frac{4}{\tau\nu}$$

or for degree measure

$$g_o \approx \frac{13131 \text{ deg}^2}{\tau\nu}$$

which gives 45.3 dB for the E- and H-plane modes and 44.3 dB for the diagonal mode. However, since we do know something about the pattern F, this is an unfair expectation of the system during scanning operation since it is still radiating the same amount of power as in the broadside case. Due to f and S_z, $F_o < 1$ away from the vertical and the intensity is lower there, which is to say that we know more power is going out in the small sidelobes. The presence of f and S_z shifts the beam slightly but has virtually no effect on beamwidth. At 30° in the H-plane, S_z lowers the gain by 0.2 dB, in the E-plane fS_z lowers it by 2.0 dB, and at 45° in the diagonal plane fS_z lowers the gain by 2.7 dB. As a reference, the optics approximation for high-gain antennas above a ground plane,

$$g_o = \frac{4\pi A}{\lambda^2}$$

where A is the aperture area seen by the observer, leads to broadside, H-plane, E-plane, and diagonal mode values of 43.9 dB, 43.2 dB, 43.2 dB, and

42.4 dB, respectively, compared to 45.8 dB, 45.1 dB, 43.3 dB, and 41.6 dB in the above considerations. Mayes (1981) shows that the conical approximation for large arrays is consistently about 1 dB too high, but as far as relative performance, a system matched for correct currents over all modes would still degrade as much as 4 dB as the last four values indicate. Matching requirements differ in different scan modes, which leads to the discussion of mutual coupling.

3.3 Effects of Mutual Coupling

Mutual coupling between elements arises due to voltages induced across element driving terminals by active radiators nearby. The superposition of all the induced voltages has the effect of altering the currents and input impedances throughout the array, which in turn affects the currents on the other radiators, etc. What is more, different scan angles must be individually dealt with, for if left alone a phased array will usually exhibit blind angles where coupling accumulation destructively notches the pattern. This "chain-reaction" type of problem quickly becomes exceedingly difficult for all but the smallest arrays. Computation is expensive enough that often not even a first-order solution is attempted and an experimental solution is sought to begin with. In the design study for the proposed large array, Tanner (1982) has written a program which begins to tackle the problem, based on the induced-emf method explained in Section 4.1.

Maximum coupling occurs in the x-direction normal to the dipoles and its worst effects have been observed in arrays which scan close to the horizon. A planar array analysis can be discussed here. The mutual impedance Z_{12} between any two elements 1 and 2 is defined as the ratio

$$Z_{12} = \frac{V_{12}}{I_2(0)} = Z_{21}$$

where V_{12} = voltage across the open-circuited terminals of element 1 induced by current on element 2

$I_2(0)$ = driving-point current into element 2

Since we need refer only to the driving points of the elements, the zero argument will be dropped. Note the negative sign customarily associated with V_{12} since the Thévenin equivalent looking into element 1 is

$$I_1^{sc} = \frac{-V_{12}}{Z_{11}'}$$

where I_1^{sc} = short-circuit current at the input of element 1 with I going into element 2 (currents going into element ports are defined positive)

Z_{11}' = input impedance of element 1 with no generator attached, and all other voltage sources shorted and current sources opened

Unless the elements are very close together, the Thévenin impedance Z_{11}' is approximately equal to the self-impedance Z_{11} defined as the input impedance of element 1 with zero driving-point currents on all others. Even with all other terminals open-circuited though, a single active element will induce currents on the others so the self-impedance varies with different locations in the array and is never exactly equal to the isolated impedance of a radiator in free space. But in the interior of a large array with identical feeds to all elements, Z_{11}' will not vary much as a function of location and may be taken as a constant to illustrate the phase addition problem.

If the Thévenin circuit described above is connected to a passive load having input impedance Z_f an induced current

$$\frac{-V_{12}}{Z_{11}' + Z_f} = \frac{-Z_{12}I_2}{Z_{11}' + Z_f}$$

will flow at the driving point of element 1. For uniform elements 1 through K which would have currents $I_1, \ldots, I_K$ in the absence of mutual coupling,

excitation in an environment with light coupling produces altered currents $I_1', \ldots, I_K'$ by superposition where

$$I_m' = I_m - \sum_{\substack{k=1 \\ k \neq m}}^{K} \frac{Z_{mk} I_k'}{Z_{11}' + Z_f} \tag{3.3}$$

and Z_f is the impedance of the feed source. It is assumed that all source impedances remain constant and equal. A matrix of coupling coefficients C_{mk} is defined by (Agrawal and Lo, 1972)

$$\begin{bmatrix} I_1' \\ I_2' \\ \cdot \\ \cdot \\ \cdot \\ I_K' \end{bmatrix} = \begin{bmatrix} I_1 \\ I_2 \\ \cdot \\ \cdot \\ \cdot \\ I_K \end{bmatrix} - \begin{bmatrix} 0 & C_{12} & \cdots & C_{K1} \\ C_{21} & 0 & & \\ \cdot & & 0 & \cdot \\ \cdot & & & \cdot \\ C_{K1} & & \cdots & 0 \end{bmatrix} \begin{bmatrix} I_1' \\ I_2' \\ \cdot \\ \cdot \\ \cdot \\ I_K' \end{bmatrix}$$

where $C_{mk} = \dfrac{Z_{mk}}{Z_{11}' + Z_f} = C_{km}$, $C_{mm} = 0$

For large arrays this is very costly to solve even if the C_{mk} are known, but since the coefficients are small compared to unity in most practical arrays, the unprimed vector can be used to multiply the coupling matrix (this amounts to a truncated Neumann series) without undue error. The ideal I_m were also used when the mutual impedances were computed, as outlined in Section 4.1.

If a planar array is given a progressive phase shift δ in an arbitrary X-direction as was done in Section 3.1, one can think in terms of a linear array with spacing d and observer angle $\theta = \theta_X$ with the X-axis. Ignoring anisotropic deviations of f and S_z, one may scale the parameters I_m, I_m' in the pattern function such that

$$I_m = |I_m| e^{j(\phi_I + m\delta)}$$

and

$$F' = \frac{1}{K} \sum_{m=1}^{K} I_m' e^{jm\beta d \cos\theta}$$

$$= \frac{1}{K} \sum_{m} (I_m + \sum_{k} C_{mk} I_k) e^{jm\beta d \cos\theta}$$

$$= F + \frac{1}{K} \sum_m \sum_k C_{mk} |I_k| e^{j(\phi_I + k\delta + m\beta d\cos\theta)}$$

where $\phi_I = -(K + 1)(\delta + \beta d\cos\theta)/2$ may be chosen to make F real.

The undisturbed pattern F is seen to be degraded by the phasor coupling expression on the right. The main beam maximum is still found as before by setting $\theta = \theta_o$ where

$$\delta + \beta d\cos\theta_o = 0$$

Then

$$F_o' = F_o - \frac{1}{K} \sum_m \sum_k C_{mk} |I_k| e^{j\beta d(m - k)\cos\theta_o}$$

as a function of scan angle θ_o, implying that the field in the main beam is no longer constant for different scan angles. Experimental evidence (Lechtreck, 1968) has shown that the phase of C_{mk} is almost exactly linear with $|m - k|$, proportional to the distance separating the elements involved. Increased spacing causes a lag in the induced response except for very close elements, whether the coupling field is radiation or a surface wave. Since V_{mk} lags I_k, a negative phase constant α is attached to C_{mk} and the pattern maximum becomes

$$F_o' = F_o - \frac{1}{K} \sum_m \sum_k |C_{mk} I_k| e^{j\alpha d|m - k| + j\beta d(m - k)\cos\theta_o}$$

which can exhibit reduction of as much as 15 dB when the scan angle makes the argument an even multiple of π. For any integer n the critical scan angles are found where

$$\cos\theta_o = \frac{2\pi n \pm \alpha d}{\beta d} = \frac{n\lambda}{d} \pm \frac{\alpha}{\beta}$$

One may try to predict troublesome scan angles by calculating C_{mk} when possible. For a very large array of dipoles $\lambda/4$ above a ground plane, the matrix of Z_{mk} ignoring secondary scattering was computed (Mayes and Tanner, 1981; Tanner, 1982) and a phase plot with respect to element spacing showed

a slope of $\alpha = -1.94\pi/\lambda$. Taking this as the phase constant of C_{mk} would lead one to believe that the critical scan angles lie about 14° above the horizon for all modes of operation of the proposed array. Although the feed system was designed to make all currents exactly $I'_m = I_m$, losses and other imperfections would probably cause problems near $\theta_o = 14°, 166°$ if anywhere. Of course it is always better to match the different driving-point impedances to the source in order to have proper element currents for all scanning modes. Feed lines with taps a half-wavelength apart connected to the elements with quarter-wave lines would result in equal element currents independent of the element impedances, in effect adjusting Z_f in C_{mk}. Coupling would be greatly reduced and there would be only four phases to worry about instead of K. The important matching would be at the four inputs to the feed lines if all elements of the same phase were connected to one of four power sources. Then the data of Table 3.1 would be valid. The details of the feed network built on this principle for the model are left to Sections 4.2 and 4.3.

4. REALIZATION OF THE MODEL ARRAY

4.1 Layout and Mounting

It was decided to model a scaled-down section of the proposed array and test it on a pattern range to monitor the directivity and sidelobes as element phasing was varied. A wavelength of 6 inches (1.967 GHz) was chosen for the UHF range atop the University of Illinois Electrical Engineering Research Laboratory. As laid out by Mayes and Tanner (1981), a square array of 64 half-wave dipoles spaced 3 inches apart was fabricated by the Electrical Engineering shop. The design consisted of a square 21 inches on a side measured between corner post centers, with 1/16 inch O.D. brass tubing elements mounted on nylon posts 1.5 inches above an aluminum ground plane. A photograph of the mounted array before the feed system was attached is shown in Figure 4.1.

For all scanning beam directions except vertical, the elements were phased at 4 different values (0°, 90°, 180°, 270°) and 16 elements would carry currents of each phase. Knowing the position and phase of each element, a computer program was used to minimize the dipole driving-point reactance in the presence of mutual coupling by fine adjustment of the dipole lengths. The mutual impedance for any element, call it number 1, in the vicinity of another element number 2 parallel to it and carrying a current I_2 is the ratio of the induced open circuit voltage across the driving point of element 1 to I_2 at the driving point of element 2. Letting both elements be oriented parallel to the y-axis, a development involving Thévenin's theorem and reciprocity (Jordan and Balmain, 1968) leads to the formula for thin dipoles

$$Z_{12} = \frac{V_{12}}{I_2(0)} = \frac{-1}{I_2(0)I_1(0)} \int_{-H}^{H} E_{y2} I_1(y)\,dy \qquad (4.1)$$

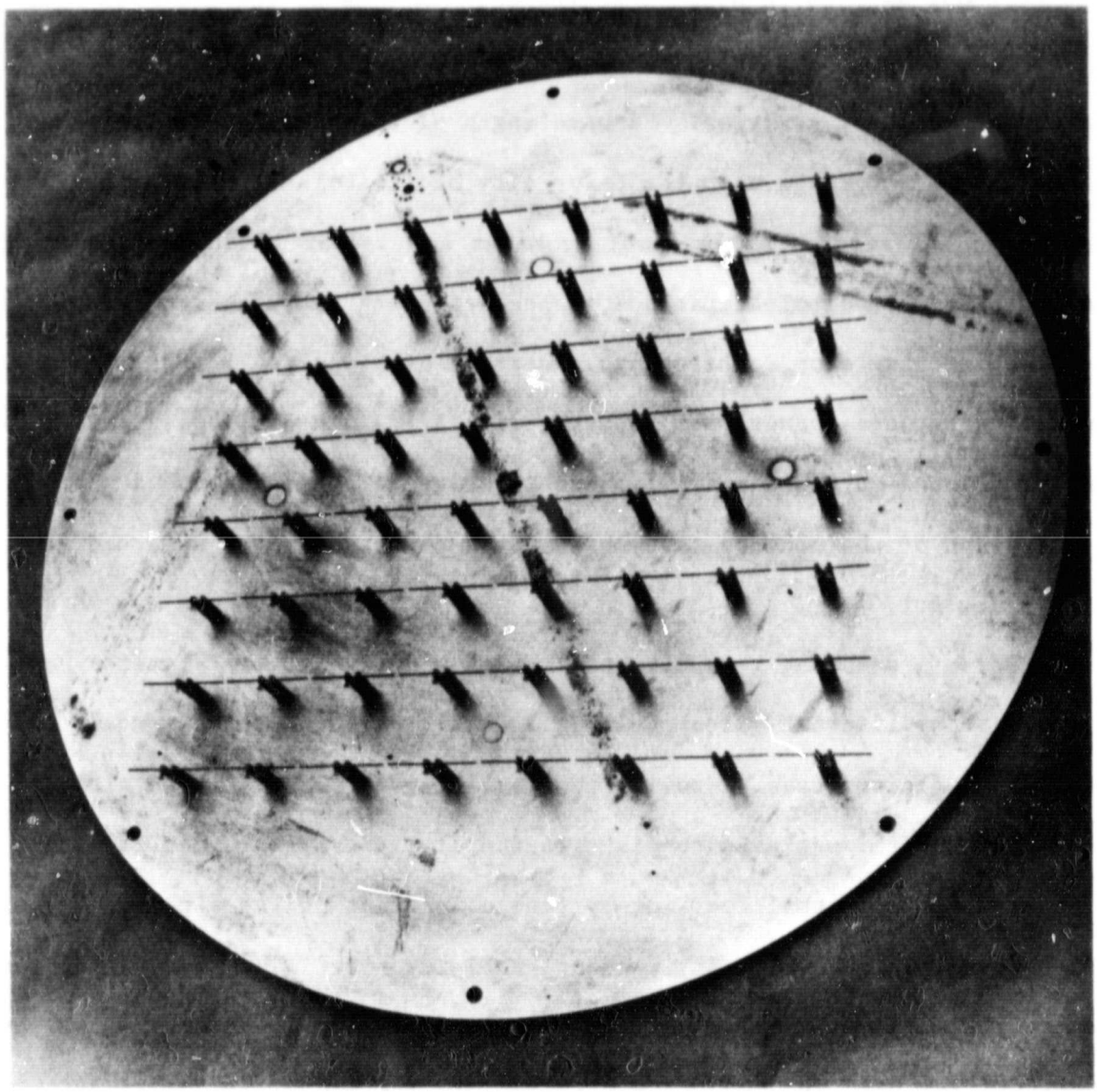

Figure 4.1 The model antenna array, scaled to λ = 6 inches.

where Z_{12} = mutual impedance of element 1 due to element 2 being driven

V_{12} = voltage across the open terminals of element 1 induced by current on element 2

$I_{1,2}(y)$ = current along element 1, 2 as a function of length on a thin wire stretching from -H to H with the driving point at the origin

E_{y2} = y- component of the electric field produced by element 2 by itself radiating in free space

A good approximation for the current on a thin wire is a distribution which is sinusoidal from the ends, expressed as

$$I_1(y) = \frac{I_1(0)}{\sin\beta H} \sin\beta(H - |y|) \tag{4.2}$$

where $\beta=2\pi/\lambda$ is the free-space wave number. Likewise, the E_y component of the near field from element 2 (same current distribution) is given by

$$E_{y2} = \frac{j30I_2(0)}{\sin\beta H} \left(\frac{2\cos\beta H e^{-j\beta r_o}}{r_o} - \frac{e^{-j\beta r_1}}{r_1} - \frac{e^{-j\beta r_2}}{r_2} \right) \tag{4.3}$$

where $r_o = \sqrt{d_{12}^2 + (\ell_{12} + y)^2}$

$r_1 = \sqrt{d_{12}^2 + (\ell_{12} - H + y)^2}$

$r_2 = \sqrt{d_{12}^2 + (\ell_{12} + H + y)^2}$

d_{12} = normal distance between element axes

ℓ_{12} = distance between element centers along the y-axis

A sketch of this configuration is given in Figure 4.2.

Given the above information, the mutual impedance between arbitrary elements was computed as the dipole length was reduced slightly from $\lambda/2$. The total driving point impedance for (an arbitrary) element number 1 near the array center arises from a matrix impedance relation and was also

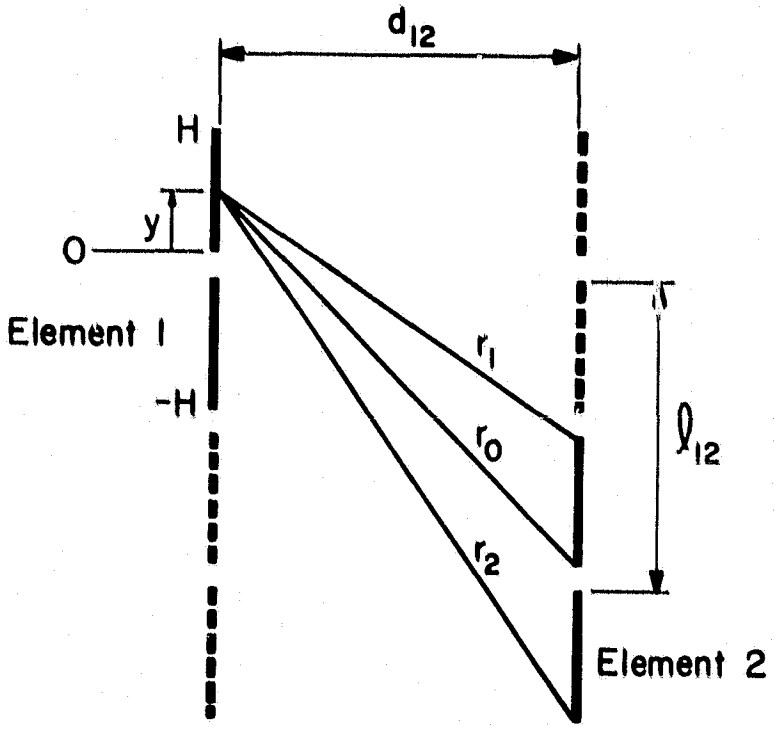

Figure 4.2 Position of elements in mutual impedance calculations.

computed as follows. Dropping the y argument (since y = 0), the gap voltages V_1, V_2,..., V_K and the driving point currents I_1, I_2,..., I_K on elements 1, 2,..., K are related by

$$\begin{bmatrix} V_1 \\ \vdots \\ V_K \end{bmatrix} = \begin{bmatrix} Z_{11} & \cdots & Z_{1K} \\ \vdots & & \vdots \\ Z_{K1} & \cdots & Z_{KK} \end{bmatrix} \begin{bmatrix} I_1 \\ \vdots \\ I_K \end{bmatrix}$$

Hence the driving-point impedance for element 1 is

$$Z_1 = \frac{V_1}{I_1} = \sum_k Z_{1k} \frac{I_k}{I_1} \quad ,$$

i.e. the sum of the self-impedance for element 1 and mutual contributions from all sources "nearby" including ideal images below the ground plane. So while Z_{11}, Z_{12},... are seen to be current-independent (Equations 4.1-4.3), the driving-point impedances are not. To faciliate computation, Z_{1k} was neglected when $|Z_{1k}| < 0.03|Z_{11}|$. A useful approximation for the self impedance of a thin cylindrical dipole of known diameter is to compute Z_{11} as if it were a mutual impedance between two line sources lying side by side, letting the separation d_{11} shrink to the cylindrical radius (1/32 inch). Considering all phasings in the environment of element 1, the optimum overall length for approximating real loads was found to be $2H = 0.47\lambda$. The self-impedance then worked out to be 65 Ω in contrast to 73 Ω for the thin $\lambda/2$ case in the absence of other elements, and the driving-point impedances varied from 100 Ω to 150 Ω. Secondary scattering from the feed lines and the elements was ignored (the approximately $\lambda/4$ lengths of tubing were assumed non-resonant), as was the 0.080 inch gap at each driving point. Although the reactance of the edgemost elements was high (on the order of 60 Ω) and virtually uncontrollable, for the more numerous interior elements of the array the maximum magnitude of the driving-point reactance was calculated as 20 Ω, and $H = 0.235\lambda$ was adopted. More information on the computer programs

which calculated the mutual and driving-point impedances can be found in Tanner (1982).

4.2 Baluns and Connections to Dipoles

In order to get from 50 Ω coaxial cable to a balanced source necessary to drive the elements a balun arrangement was needed. Because of the availability of low-loss Rexolite circuit board and ease of construction, the half-wave microstrip balun (assumed lossless) was etched on 1/16 inch Rexolite, the line length curved back such that a balanced voltage with respect to ground was formed across the gap. As seen in Figure 4.3, the two taps at V and -V amount to a balanced power source when the balun is fed at one end and connected to balanced loads Z_L. If the length of the balun is $\lambda/2$, half of the effective wavelength in the microstrip, the end voltages must be equal and opposite for any real characteristic impedance Z_o. We then assume equal and opposite currents through the loads Z_L. Note that as a function or length x, the line current I(x) by inspection is found to be

$$I(\lambda/2) = -V/Z_L = -I(0^+)$$

and

$$I(0^-) = I(0^+) + V/Z_L = 2I(0^+)$$

This behavior can also be seen from the matrix for uniform lossless lines

$$\begin{bmatrix} V(x) \\ I(x) \end{bmatrix} = \begin{bmatrix} \cos\beta x & -jZ_o \sin\beta x \\ -jY_o \sin\beta x & \cos\beta x \end{bmatrix} \begin{bmatrix} V(0) \\ I(0) \end{bmatrix} \qquad (4.4)$$

where $Y_o = 1/Z_o$ and $\beta = 2\pi/\lambda$ is the wave number of the line.

Since the loads are two-wire lines ending in antenna elements, the assumption is reasonable that they are balanced. To assure equal and opposite currents at the driving point of a center-fed element, a quarter-wave transformer was desired between balun and dipole. However, since two elements 12 inches apart were driven in parallel from one balun, two lines of length

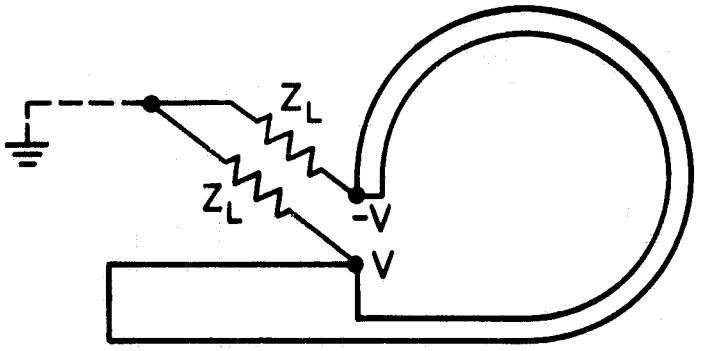

(a)

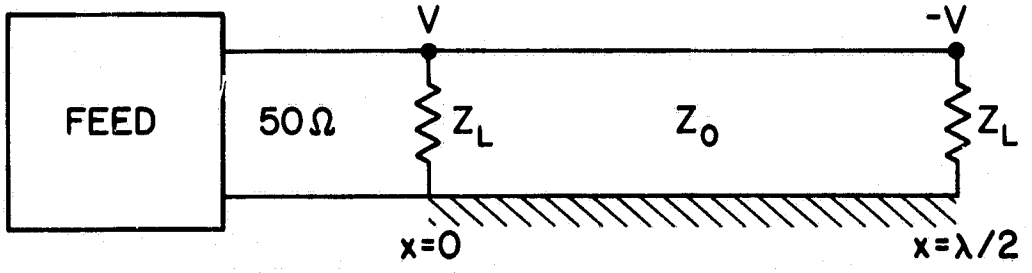

(b)

Figure 4.3 Half-wave microstrip balun (configuration above ground plane) and transmission-line circuit.

$7\lambda/4$ were used which accomplished the same thing (Equation 4.4 implies $I(7\lambda/4)$ dependent solely upon $V(0)$ and Z_o). Figure 4.4 shows one of the two identical $7\lambda/4$ lines ending in a dipole and its equivalent impedance. The other dipole is driven in parallel from the same taps and carries the same current. As indicated, a quarter-wave transformer inverts the normalized impedance Z_d/Z_o. If only the top half of the system is considered as existing above a perfect ground plane precisely in the middle of the $7\lambda/4$ line, an equivalent system as in Figure 4.4 is created with the same current but with the voltage to ground only half of that across the line. Thus the balanced feed can be treated as two unbalanced circuits if desired, with the characteristic and "looking-in" impedances halved. The unbalanced approach involves the quarter-wave monopole and its image.

If a load was connected to a balun as in Figure 4.3a with the center tap left floating, a perfect balun would produce zero voltage at the midpoint. A preliminary test was made on a Hewlett-Packard s-parameter test set with a balun connected to two 100 Ω (5%) resistors as in Figure 4.5. Subscripts refer to ports, and superscripts to incident or reflected traveling waves. When power was fed into port 1 at the design frequency of 1.967 GHz the resulting output from port 2 was found to be about 24 dB down, thus verifying the balun's experimental performance.

According to the aforementioned program, the actual driving-point impedances of the elements varied from about 100 Ω to 150 Ω due to mutual effects. The maximum reactance except at the edges was less than 20 Ω. In order to minimize reflections it seemed expedient to try to make Z_o and Z_L in Figure 4.3b equal to 100 Ω. Therefore the total balanced load on the balun would be 200 Ω.

Each balun was wired to two dipoles separated four elements (2λ) apart,

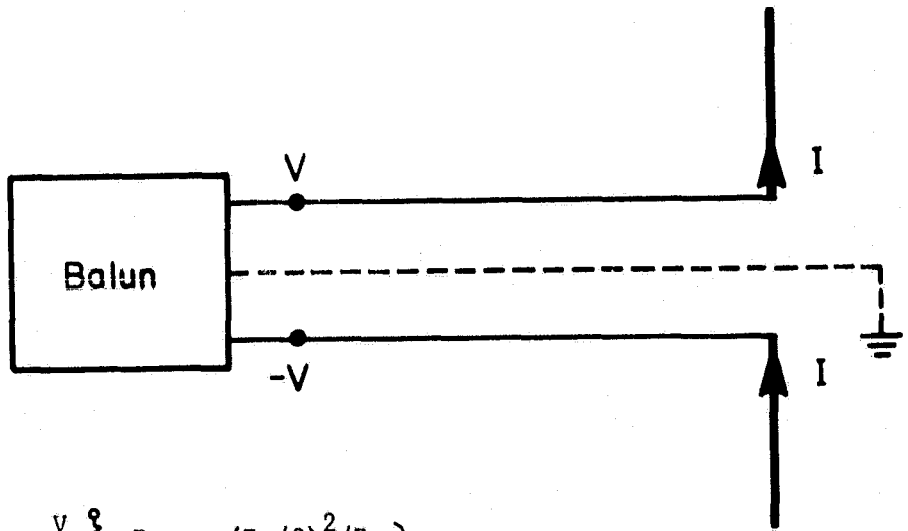

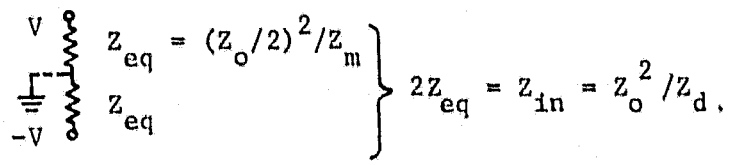

Figure 4.4 Balanced element feed line showing input impedance, where

Z_{eq} = equivalent input impedance for unbalanced case

Z_d = driving-point impedance of dipole

$Z_m = Z_d/2$ = driving-point impedance of monopole

Z_o = characteristic impedance of balanced line

Z_{in} = input impedance of balanced circuit

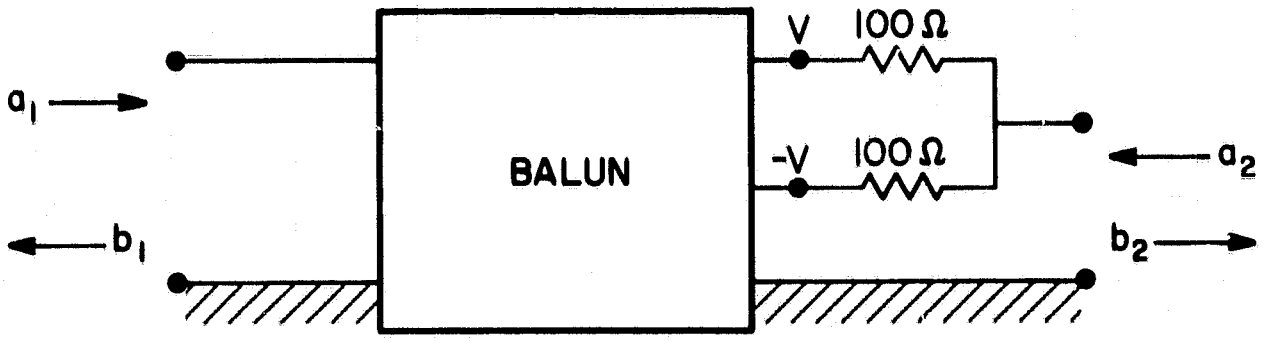

Figure 4.5 Balun test setup, where

$a_{1,2} = V^{inc}_{1,2} / \sqrt{Z_o}$

$b_{1,2} = V^{refl}_{1,2} / \sqrt{Z_o}$

$Z_o = 50\Omega$ = characteristic impedance of lines connected to test set

S_{21} = forward transmission coefficient into a matched load (no reflections)

$|S_{21}|^2$ = forward power gain

two $7\lambda/4$ transformer lines driven in parallel as shown in Figure 4.6, and we may assume that the shared voltage at one end resulted in equal currents at the other. For the input impedance of each line to be 400Ω a line impedance of about 224 Ω was desired, i.e. the geometric mean of 400 Ω and an intermediate dipole impedance of 125 Ω. "Twin-lead" cut from Teflon-insulated ribbon cable was found to exhibit a uniform 190 Ω on a time domain reflectometer. When this material was shorted at one end and the other end was connected to one port on the s-parameter test set, measurements of the reflection coefficient ($s_{11} = b_1/a_1$) along the line showed an effective wavelength of 4.14 inches at 1.967 GHz, or a velocity factor of 0.69, without appreciable losses over the length needed. Sixty-four $7\lambda/4$ transformers were then cut at 7.25 inches apiece, and since there was no great power requirement the small mismatch was acceptable.

As for the microstrip itself, knowing that Rexolite has a relative dielectric constant of 2.62 one can synthesize 50 Ω and 100 Ω line on 1/16 inch thick board using Hammerstad's formulas (Hammerstad, 1975) or tables as shown in Table 4.1. Hammerstad's formulas are quite tedious and most practical applications can be taken from either tables or graphs. The plots are improved versions of the more familiar Wheeler curves and their development was based upon Wheeler's earlier work (Wheeler, 1965). The interested reader is referred to the References. A half-wavelength of 100 Ω strip is therefore 3 x 0.173 = 2.14 inches, and baluns were made with the line shaped into a smooth curve as sketched in Figure 4.3. Each group across the ends was about 3/16 inch, or a little more than the width of the adjacent 50 Ω section to which the coaxial feed was soldered.

4.3 Multi-Port Phased Source

A prominent feature of the power network for the model is the trans-

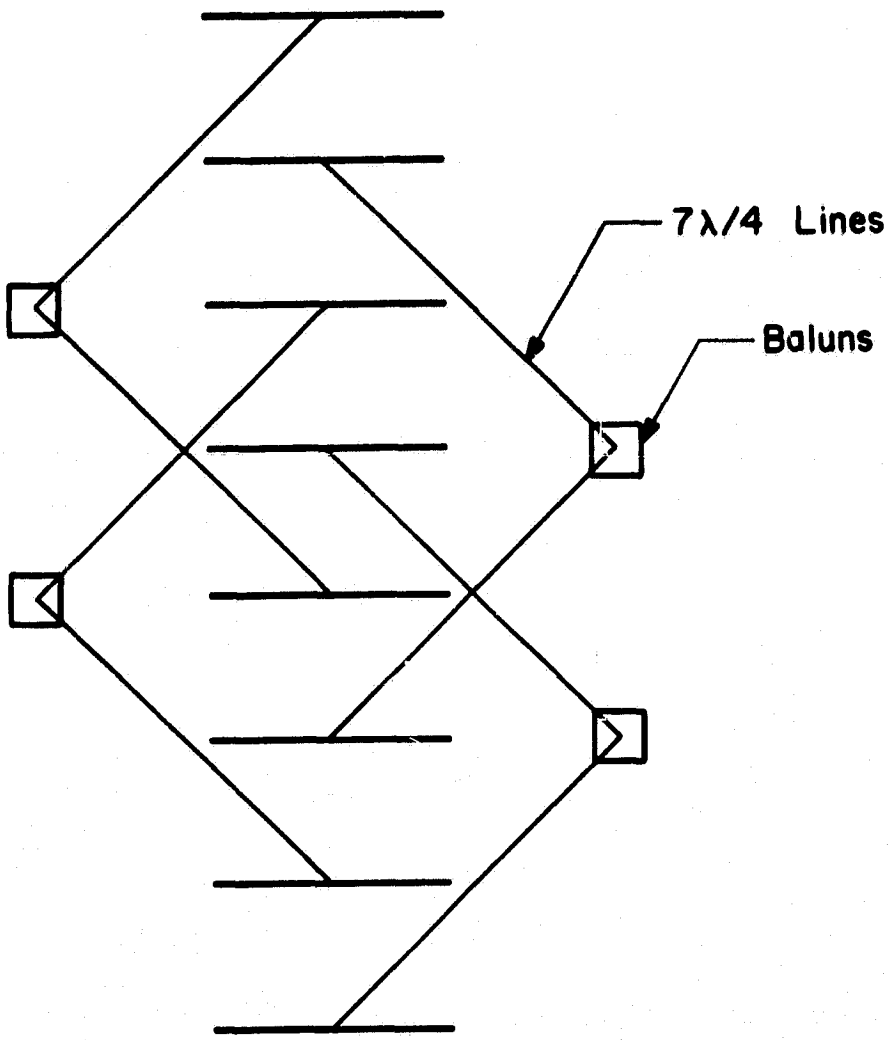

Figure 4.6 Four baluns connected to a row of dipoles.

Table 4.1 Microstrip parameters for 1/16 inch Rexolite circuit board.

Z_o	strip width	velocity factor
50 Ω	0.166 inch (4.2 mm)	0.688
100 Ω	0.045 inch (1.1 mm)	0.713

mission line half-wave transformer. No matter how terminated, a lossless line exhibits a repeated voltage (and current) every half-wavelength along itself, with alternating polarity at each successive point. As predicted by Equation 4.4, V transforms to V at a distance of λ, 2λ, 3λ,... and $-V$ at $\lambda/2$, $3\lambda/2$, $5\lambda/2$,... Consider a group of 16 elements in phase, or 8 ports into the 8 baluns used to drive them. Since we wanted equal V and $-V$ on each balun (Figure 4.3, 4.4) a straightforward method of connecting 32 equivalent half-wave lines in parallel to a common source point was used. Each equivalent line consisted of a length of RG-58/U coaxial cable (Z_o = 50 Ω) soldered directly to a balun input at one end while the other end was able to be attached, with type-N connectors, to a microstrip matching network that branched out 8 ways from the common source. The total electrical length from the output of this microstrip network to the nearer tap on the balun was made to be an integer number (18) of half-wavelengths. The actual length through cable and connections was set with the aid of the s-parameter equipment to be 35.75 inches.

A sketch of the branched microstrip configuration that was realized with copper tape on 3/16 inch Rexolite is given in Figure 4.7. Four of these networks were made. The feed point is at 0 in the figure, and when the 8 outputs are connected to 50 Ω each, every fork in the network has two 100 Ω impedances in parallel from the effect of quarter-wave transformers in series. At the points in between forks where the strip changes width, the impedance looking towards the load was arbitrarily set at 70.7 Ω by interposing a $\lambda/4$ strip of uniform characteristic impedance $\sqrt{70.7 \times 50}$ = 59.5 Ω A narrower strip was then placed in series having a characteristic impedance of $\sqrt{100 \times 70.7}$ = 84.1 Ω so that the parallel connection shown could achieve another 50 Ω load. Table 4.2 gives the microstrip parameters

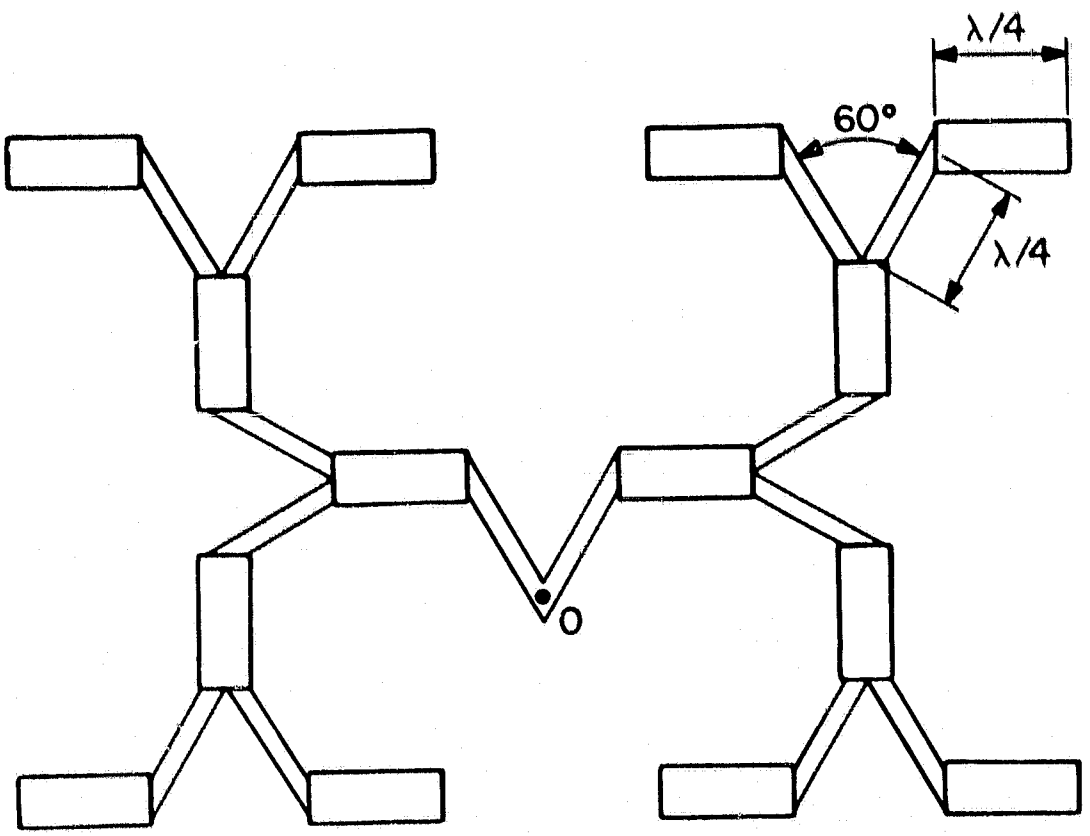

Figure 4.7 Microstrip configuration in one of four identical branching networks.

Table 4.2 Microstrip parameters for 3/16 inch Rexolite circuit board.

Z_o	strip width	$\lambda/4$
59.5 Ω	0.374 inch (9.5 mm)	1.04 inch (26.4 mm)
84.1 Ω	0.193 inch (4.9 mm)	1.06 inch (26.9 mm)

including the effective quarter-wavelength along the centerline of each piece. This series of $\lambda/4$ sections guarantees equal voltage at the output ends of the network as long as the branching proceeds through identical stages, since cascading (multiplying) the transmission matrices (Equation 4.4) of all the $\lambda/4$ sections produces the same expression for the voltage at all 8 outputs regardless of current.

Due the effect of these "power splitters" connected to the half-wave transformer coaxial lines, half-wave baluns, and quarter-wave transformer twisted lines, equal voltages at the four power-splitter inputs should result in equal currents on every element in the array. This was done to produce a beam normal to the array by connecting each 8-way power splitter to a driving 4-way splitter of the same design. It was possible to connect the 4-way to the 8-ways using the type-N connectors only (without cables) and all four electrical lengths were made equal. The power-splitter setup for transmitting a broadside beam is sketched in Figure 4.8 in which it is understood that there is a total of 32 baluns connected like the one shown.

There are slight mismatches due to the variable driving-point impedance, but the fact that 16 elements are covered by each 8-way network would approximately equalize the four loads as seen from the 4-way splitter. The voltage standing wave ratio at that point would be only about 1.2 or less. Equal loads would ideally mean equal voltages at the 8-way inputs, and good results (a well defined beam) were obtained with no further matching required. When the 4-way network was replaced with commercial phase-shifting hybrids and the proper phase sent to each element, the beam was satisfactorily scanned. The three available hybrids were 4-port couplers terminated in 50 Ω dummy loads, two 180° couplers manufactured by Alford and a 90° coupler by Narda. The progressively phased power source was connected as in

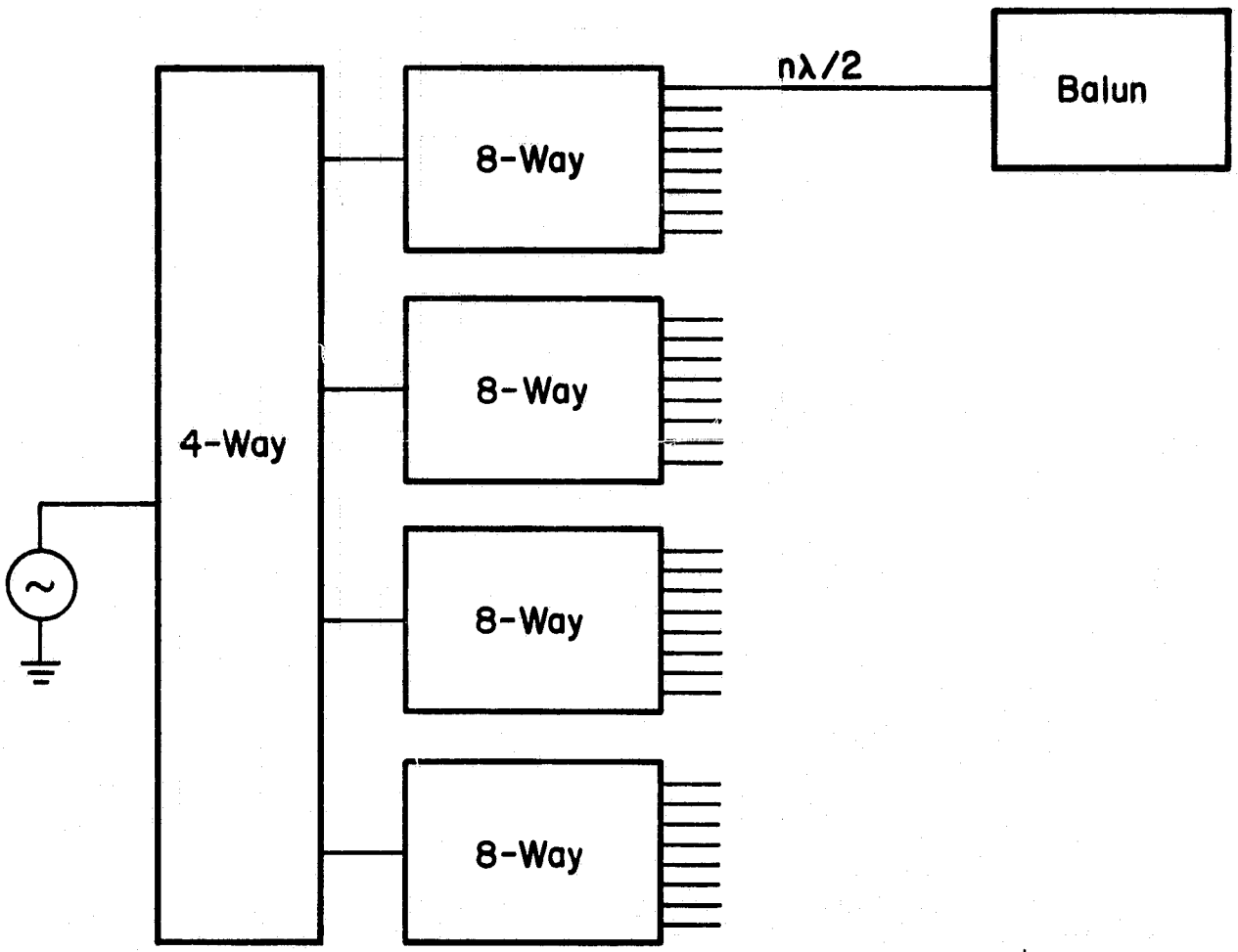

Figure 4.8 Power-splitter connections for in-phase currents on all elements, where nλ/2 denotes an electrical path of an integer number of half-wavelengths.

Figure 4.9. The outputs were essentially quadriphase 50 Ω Thévenin sources, and the averaging effect of the 8-way connections assured approximately equal loads and proper operation for all scanning modes. Mutual coupling would theoretically superimpose a further mismatch at the elements to increase initial transients going back into the feed system. However, after stabilization the effect of half- and quarter-wave transformers should be to lock all the currents of one phase to their proper values, providing that mutual effects do not unbalance the elements or couple too much into the feed network above the ground. Taking mutual impedances into account, hopefully the worst that could happen would have been a need to equalize the four inputs seen by the hybrids in Figure 4.9.

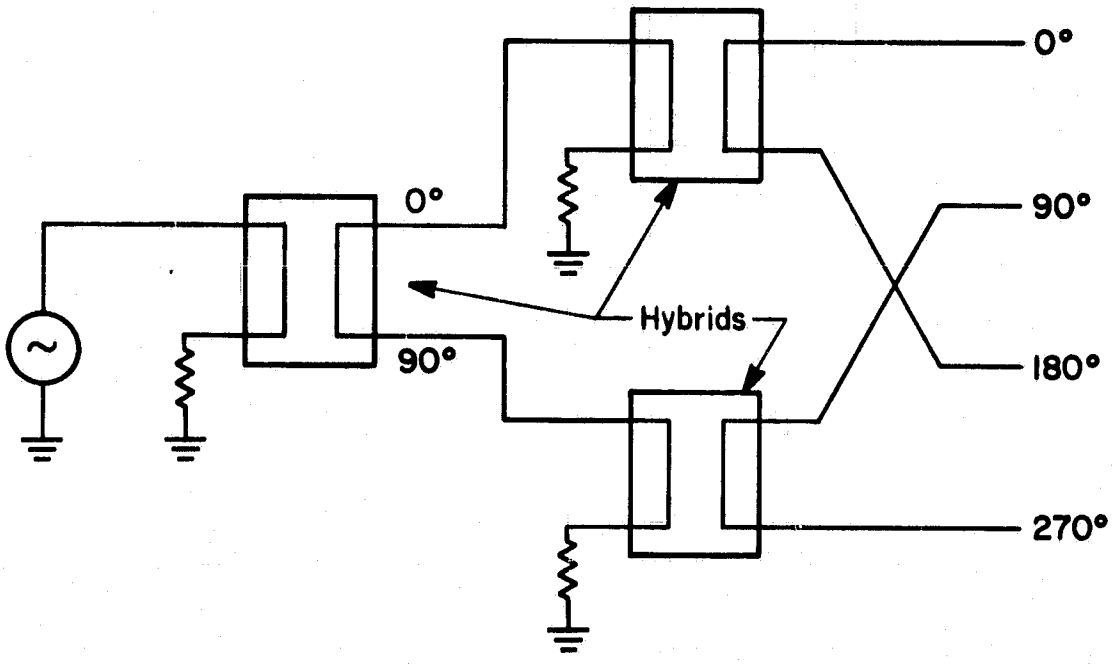

Figure 4.9 Hybrid realization of 4 phased sources to drive 8-way power splitters.

5. EXPERIMENTAL SETUP

5.1 Transmitter

The outdoor UHF range at the University of Illinois is accessible from the roof of the Electrical Engineering Research Laboratory. The aluminum roof of the range itself serves as a ground plane, a level square about 20 feet on a side. A turntable approximately 3 feet across is set in the center for mounting the antenna under test, providing azimuthal control. Far-field radiation may be received by a probe antenna on a fiberglass boom which extends about 15 feet and swings overhead in the east-west plane, providing elevation control. The probe used for these experiments was a 3 inch dipole mounted in a corner reflector, both rotatable as a whole by a servo in order to set the polarization.

A block diagram of the transmitter apparatus is quite explanatory and is sketched in Figure 5.1 along with a list of manufacturers and model numbers. The power oscillator was a mechanically adjustable cavity type, very narrowband (less than 3 MHz wide), capable of about 5 W average output at 1967 MHz, with a built-in modulator set for a 400 Hz square wave (the receiver also uses a diode detector, which will not register without modulation). After filtering out higher UHF harmonics from the cavity, a triple-stub tuner was used to insure maximum power to the load, adjustable by watching the amplitude on the receiving plotter. A small amount of power was also coupled away from the main feed by a directional coupler tee equipped with BNC connectors and an adjustable attenuator at the low level output. The UHF frequency and modulation waveform could be continually checked by a cavity-type frequency counter and an oscilloscope fed by an envelope detector. The cavity was accurate to within ± 1 MHz. The detector used was one of the small in-line square-law diode types fitted with type-N

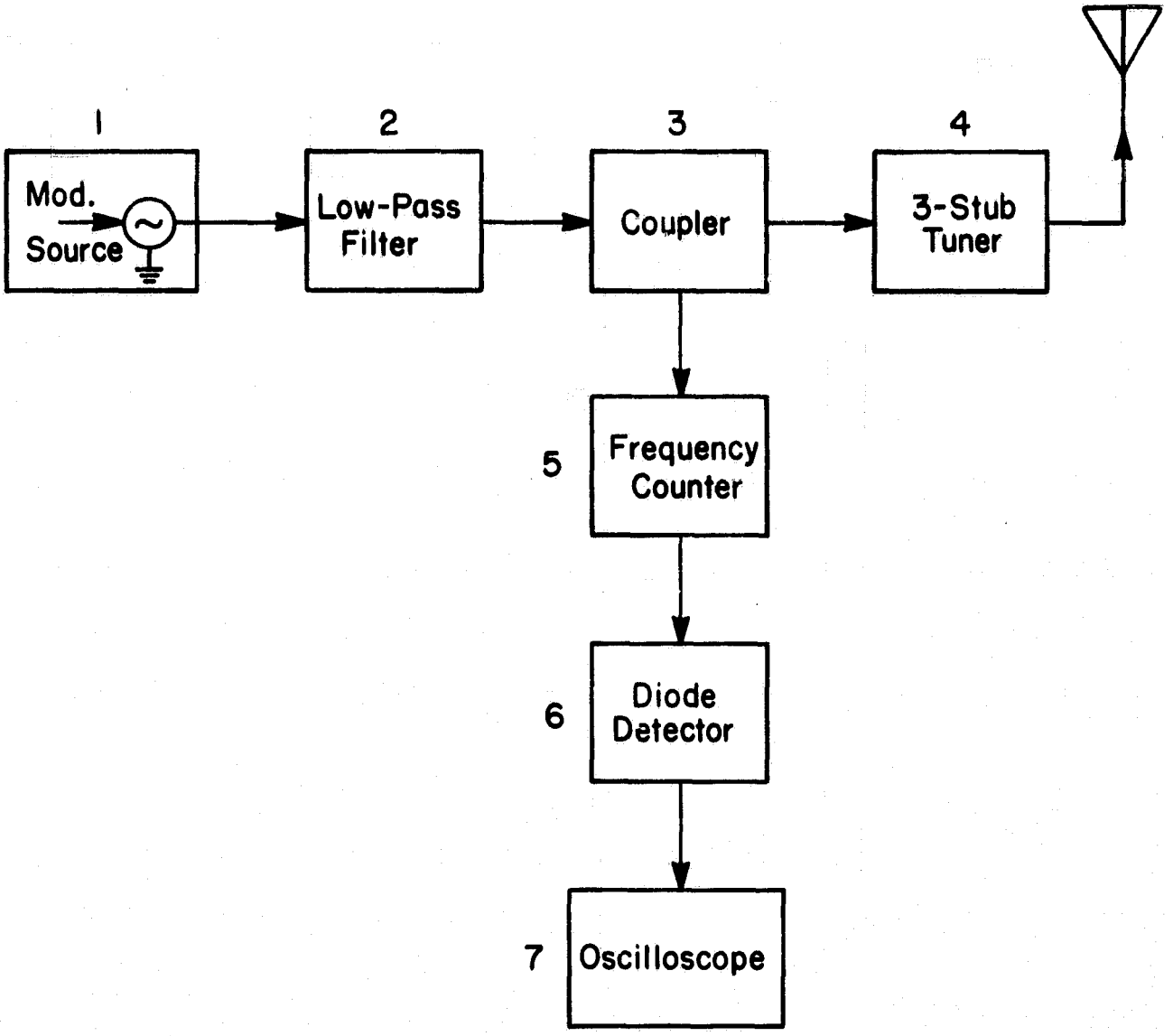

Figure 5.1 Transmitter system components

(1) Airborne Instruments Laboratory Type 124
(2) coaxial connector type
(3) General Radio Type 874-GA
(4) General Radio Type 874-D50L
(5) FXR N410A
(6) coaxial connector type
(7) RCA WO-33A

connectors. All UHF connections were made with RG-8/U lines and BNC connectors up to the feed network of the antenna itself.

5.2 Receiver

A block diagram of the receiver section of the range is given in Figure 5.2. An elevation and azimuth control unit moves either the boom with the probe antenna or the turntable and transmitting device, according to a selector switch. Either one or the other type of motion is transferred to the graph paper, which rests on another smaller turntable on the polar plotter. Polarization of the probe is also controlled from the elevation and azimuth unit but there is no corresponding hookup to the plotter. The diode envelope detector was originally placed indoors (under the ground plane) with another stub tuner inserted between it and the dipole probe. Even with the transmitter off and the probe disconnected however, the long length of RG-8/U between it and the tuner seemed to pick up low-frequency noise, perhaps from nearby power equipment, which showed on the plotter. A better SNR resulted when the diode was placed on the boom connected immediately behind the dipole and the tuner was eliminated. An audio amplifier with controllable gain then boosted the signal to the mechanical plotting pen.

Although the diodes used were square-law detectors, the plotting apparatus was equipped with a linear, square root, or logarithmic selector. Field-strength patterns were therefore facilitated with the square root setting. A bolometer was also available but it turned out to be a much noisier detector. Evidence of saturation was noted when the transmitting power was maximized, i.e. the voltage out of the detector no longer increased proportionally as the power in, but some experimentation with lower power levels on the cavity oscillator and another TWT amplifier produced a good linear response. Such a setting (1 or 2 W) was then used throughout the experiment.

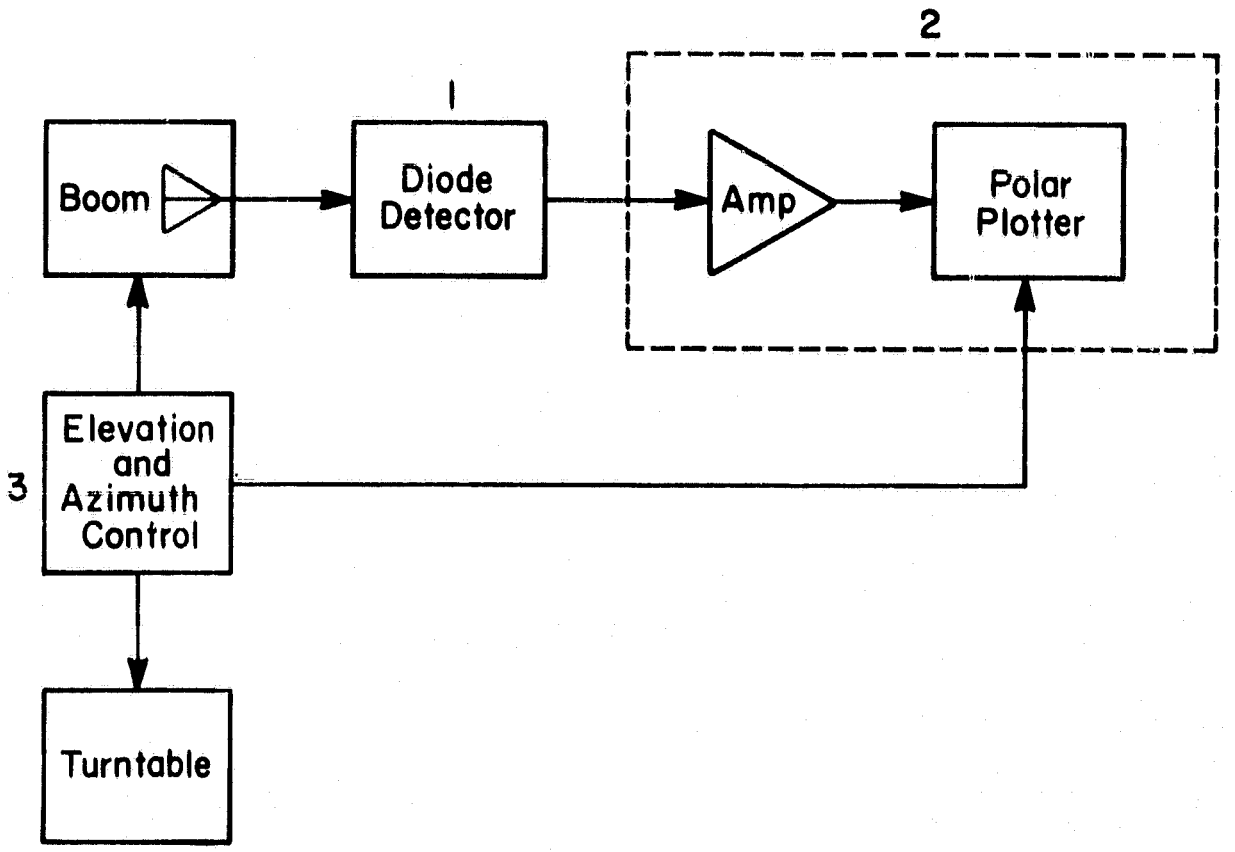

Figure 5.2 Receiver system components

(1) coaxial connector type

(2) Scientific-Atlanta Series APR 20/30

(3) Scientific-Atlanta Series PC4

6. RESULTS

6.1 Experimental Patterns and Interpretation

The 8 x 8 element model array was tested on the UHF rooftop range at the Electrical Engineering Research Laboratory at 1967 ±1MHz with the transmitter at less than 2 W at all times. Experience with the range has shown that good linearity is achieved with the available small type-N connector diode detectors at very low transmitter power, set just high enough to produce a plot of the signal above the noise level. Considerable tuning was required to keep the transmitter operating and to get good reception after connecting and reconnecting the feed lines. In addition, some plotted signal fluctuations on the order of ±0.3dB were noticed over long operating periods (more than 1 hour), so absolute field patterns in different scanning modes were not trustworthy. For the shorter time needed to take relative patterns however, the levels were fairly constant and relative plots could be taken to within ± 0.05 dB accuracy. Angular coordinates on the polar plots are lagging about 1.5° behind the direction of pen motion relative to the paper, due to mechanical backlash which showed the worst effects in the outer third of the graph paper. Although some distortion results from this the plots are apparently only shifted, within ±1° of where they should be before shifting. In the following principal plane graphs, the motion of the recording pen as seen by the paper is shown by arrows. A square-root setting was selected on the plotter and all recordings are field-strength patterns.

Figure 6.1 through 6.5 are the patterns obtained by elevation sweeps for all possible E- and H-plane scan angles including broadside, and although the ±30° beams on either side of the vertical should be identical by symmetry, the fact that they were not exactly so would lead one to suspect phase errors distributed through the feed system rather than mutual coupling.

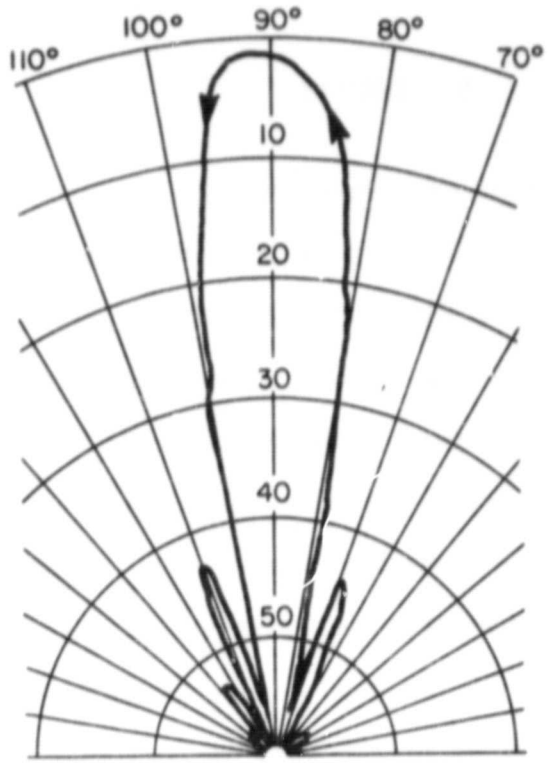

Figure 6.1 Model E-plane pattern, broadside.

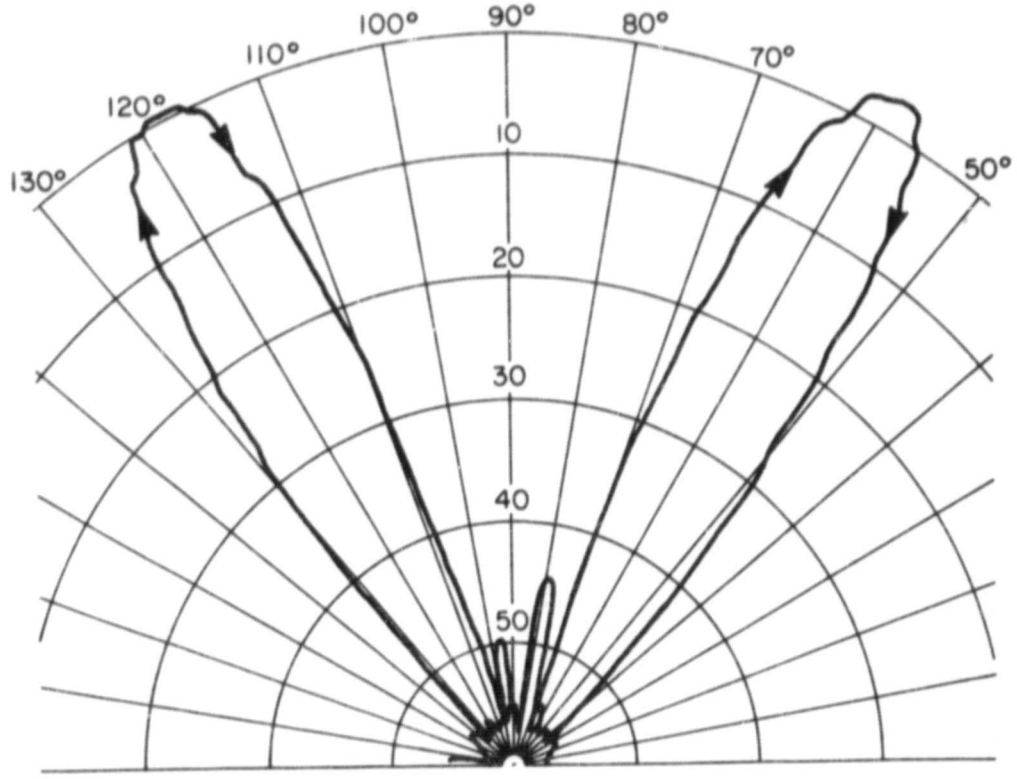

Figure 6.2 Model E-plane pattern, displaced±30°.

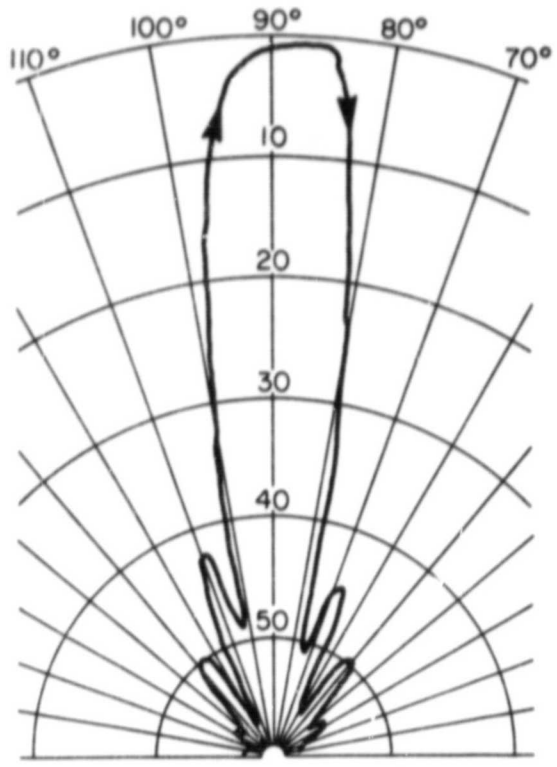

Figure 6.3 Model H-plane pattern, broadside.

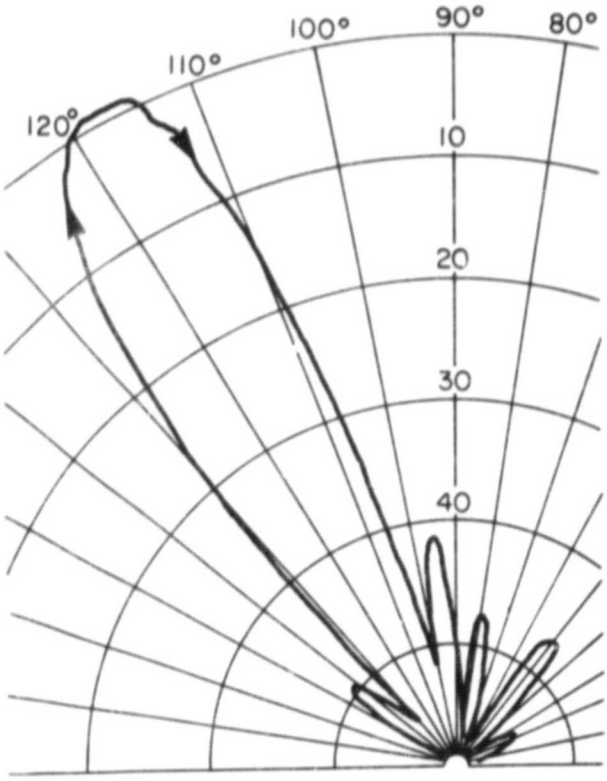

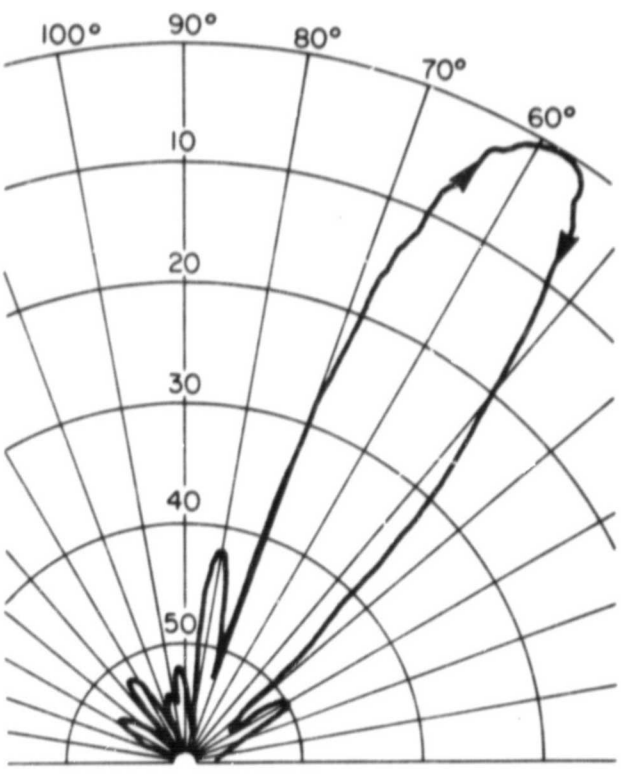

Figures 6.4, 6.5 Model H-plane patterns, displaced ±30°.

Some mutual effects were apparent in the H-plane, for the nulls in Figures 6.4, 6.5 were not nearly as close to zero as in the E-plane, which was scanned in the same manner. These effects probably account for the wider beamwidth in the H-plane which covers about 18° instead of the 14.7° predicted in Table 3.1, which may be compared to the exhibited 15° and theoretical 14.1° beamwidth in the E-plane. Broadside plots shown in Figures 6.1 and 6.3 have beamwidths of 17° in both E- and H-planes whereas theory predicts 12.6° and 12.8°, respectively.

Azimuthal E-plane plots were taken for a beam scanned at $\theta_{yo} \approx 60°$. The array was rotated on a turntable while the receiver was positioned at θ_z values from 20° to 40°. Figure 6.6 shows the results of this. The vertical line of the graph paper corresponds to $\phi = 90°$, and the various θ_z angles are marked in the lobe tips. By plotting half-power and quarter-power points on the θ_z versus ϕ graph of Figure 6.7 one can see an almost circular conical beam with total beamwidth of 15°, the same as in Figure 6.2. A ϕ range of 30° at $\theta_{yo} = 60°$ corresponds to about 15° as seen from the origin. As in Section 3.1, θ_y deviations from a great-circle sweep through the E-plane value θ_{yo} are small, since a ϕ offset if 17° from the E-plane ($\phi = 90°$) along a constant $\theta_{zo}=30°$ increases θ_y by less than 1.1° from its ν-plane value at the same ϕ. A glance at Figure 6.1 shows that the change in the Sy-dominated pattern within ±1.1° of the tip is hardly noticeable. More precisely, given an elevation $\theta_z = \theta_{ze}$ at $\phi = 90°$, the ν-plane relation through that point is

$$\frac{\cos\theta_{y\nu}}{\sin\theta_{x\nu}} = \sin\theta_{ze}$$

in this region, where $\theta_{x\nu}$ and $\theta_{y\nu}$ define the ν-plane (for lateral beamwidth calculations). Since it is true everywhere that

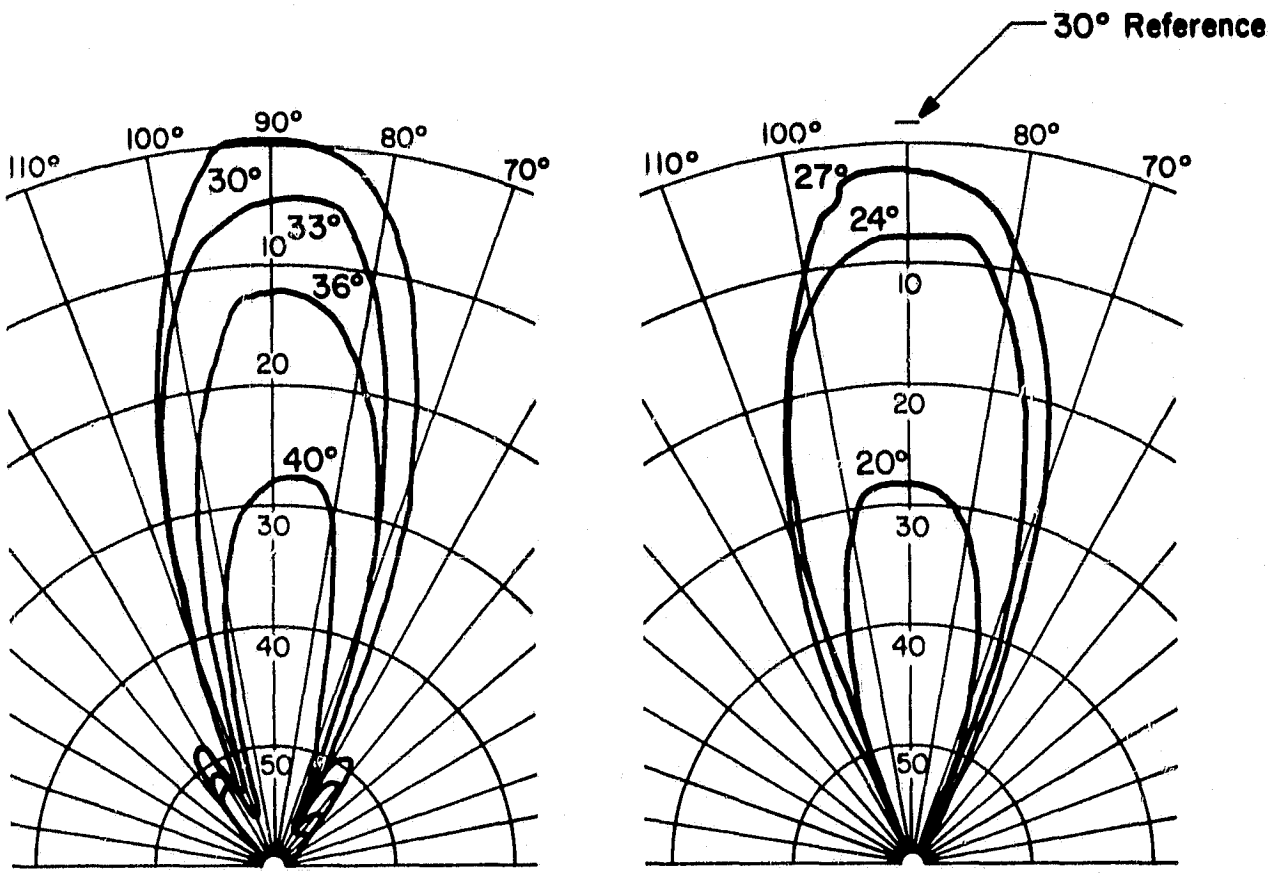

Figure 6.6 Model azimuth patterns for various θ_z settings, E-plane beam displaced 30°.

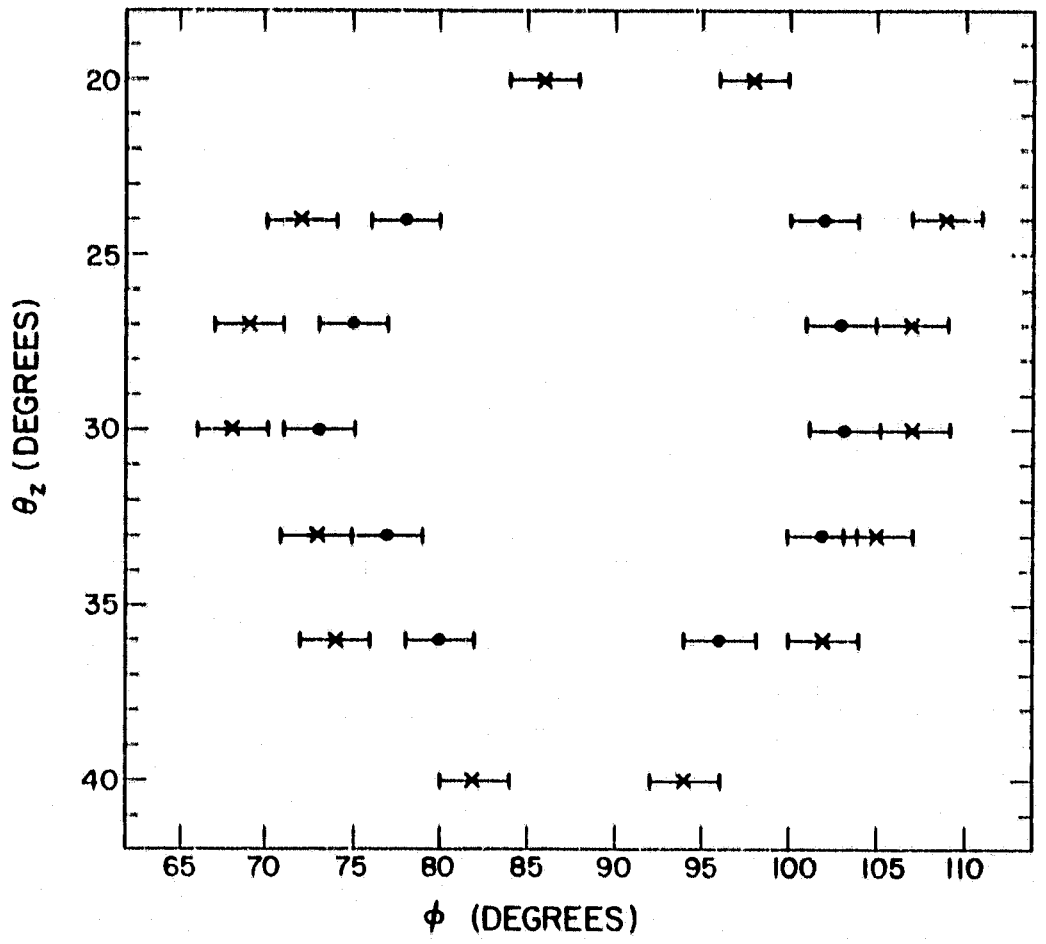

Figure 6.7 Half-power (dot) and quarter-power (x) points of E-plane beam displaced 30°, plotted in θ_z and ϕ.

$$\cos\theta_x = \sin\theta_z\cos\phi$$
$$\cos\theta_y = \sin\theta_z\sin\phi \qquad (6.1)$$

then one can determine the magnitude of θ_x and θ_y deviations, because as ϕ moves along a constant $\theta_z = \theta_{ze}$ (azimuthal plot) Equations 6.1 give θ_x and θ_y there while the ν-plane values for the same ϕ would be

$$\tan\theta_{x\nu} = \frac{\tan\phi}{\sin\theta_{ze}}$$
$$\cos\theta_{y\nu} = \sin\theta_{x\nu}\sin\theta_{ze} \qquad (6.2)$$

The difference $|\theta_x - \theta_{x\nu}|$ is less than a third of the $|\theta_y - \theta_{y\nu}|$ deviation at the edge of the E-plane beam of Figure 6.7, and even for a beam this wide, the lateral displacement $\Delta\theta_x \approx \Delta\theta_{x\nu} = \Delta\nu \approx \sin\theta_{ze}\Delta\phi$ away from the z-axis. (The angle ν seen from the origin is defined in Section 3.1. If one desires to generalize Equations 6.2 to arrays scanned in the positive X-direction as in Section 3.1, then for $\phi = \phi_X$ referred to the X-axis, it is necessary to change the subscripts y to X and x to Y and to rewrite the first of Equations 6.2 as $\cot\theta_{Y\nu} = \tan\phi_X \sin\theta_{ze}$.) So since the patterns depend heavily upon θ_x and θ_y, the constant θ_z beamwidths are useful for our purposes and the picture given by Figure 6.7 is essentially correct. Sidelobes appear in Figure 6.6 below the beam and off to the side as theory predicts since θ_y approaches θ_{yo} there. The theoretical beamwidth in the ν-plane is approximately 12.8°, the same as in the broadside H-plane.

Up to this point all polarizations of the receiving antenna have been collinear with the radiated E-vector. For the diagonal scan mode this was not possible because the polarization of the probe set parallel to the dipoles overhead became tilted as the boom was lowered in the elevation plane. With the probe set parallel at $\theta_z = 0°$, the plots in Figures 6.8, 6.9 were recorded showing obvious beams at ±45° on either side of the vertical. The probe was again run through the elevation plane at orthogonal polariza-

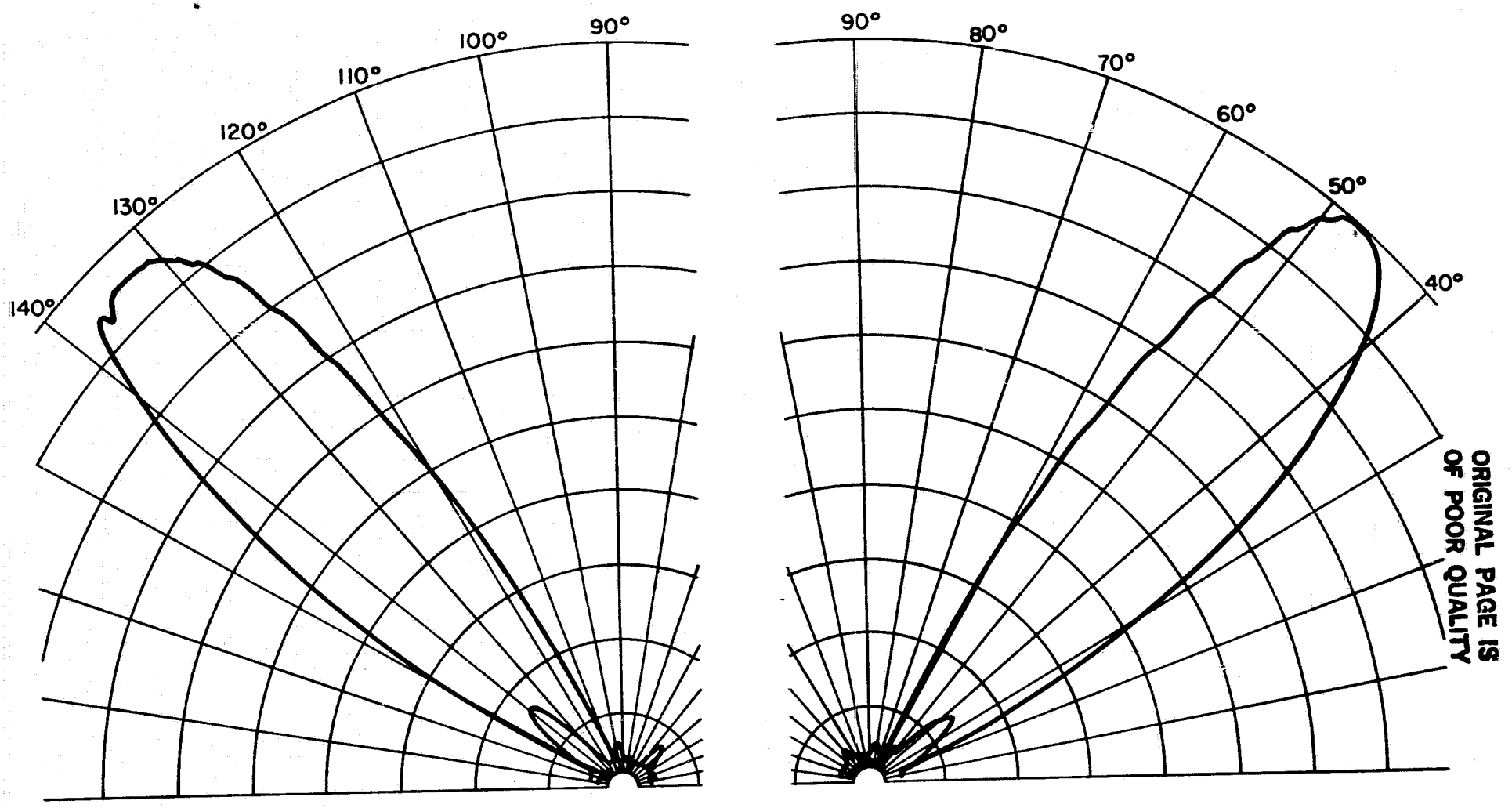

Figures 6.8, 6.9 Model diagonal-plane patterns, displaced ±45°.

tion and the plot of the received power is shown on the graph paper as small fingers inside of the large beams. When the powers (squares) are added, the main beams are essentially unchanged, growing longer by only around 0.3 dB. Elevation beamwidth is about 20° experimentally compared to 17.2° in Table 3.1, and most sidelobes in this plane are so small as to be lost in the noise. As mentioned earlier the largest sidelobes would be expected elsewhere.

6.2 Error Defects In Patterns

Since element locations and heights seem very accurately laid out by the shop (see Figure 4.1), we may assume that the spreading of beamwidths from their theoretical values was caused by errors in the currents on the elements, most importantly by phase errors rather than magnitudes (Weeks, 1968). A 22% error increase in the H-plane beamwidth for the ±30° modes is probably indicative of mutual coupling since that is the direction of maximum coupling between dipoles, and because the hybrid source in Figure 4.9 was better machined than the 4-way power splitter of the broadside mode which utilized (imperfect) half-wave transformers. Broadside operation was achieved by replacing the H-plane phased hybrid setup by the 4-way power splitter. A random hookup of the 32 feed cables would have surely led to a more uniform current distribution, since in H-plane phased operation (phase shift δ_x) two of the four loads contain all of the y-directed edge row elements, the two rows most affected by mutual effects since they are receiving them broadside. In the E-plane (δ_y) phased setup on the other hand, the hybrid source is guaranteed more even loading since each x-axis column contains two broadside edge elements and the same distribution along the direction of maximum coupling. The increase in the beamwidth during broadside operation was about 35% in either principal plane, but during E-plane

phasing it was only 6.4% above theoretical measured in the elevation, undoubtedly due to more even loading in the presence of coupling. The redidual 6.4% beamwidth spread was probably due to both y-directed coupling and imperfections in the feed system between the hybrids and the elements. The 17% lateral beamwidth increase seen in the azimuthal plots is due to non-ideal currents on dipoles in x-directed columns, although the error is not as great with the hybrids as with the broadside 4-way hookup. The beamwidth of the ±45° beams in the diagonal plane was increased 16%, probably indicative of an amount of coupling between the E-plane (best) and the H-plane (worst) scanned directions. A summary of these results is provided in Table 6.1. Some plots had more noise than others, visible as a hub around the center of the graph. Most of it is received noise over a much greater bandwidth than the signal and does not add coherently with the signal power. Therefore the observed field strength on the plots has not been appreciably increased by the noise.

To get an idea of the error introduced into the pattern by distributed excitation errors alone, the expression given by Ruze (1966) states that the directivity in a large array whose element currents contain independent and identically distributed Gaussian zero-mean phase errors with variance σ^2 (σ in radians), is decreased from the ideal g_o by

$$g_\phi = g_o e^{-\sigma^2}$$

if the errors are not too large.

Also available (Jasik, 1961) is the approximate degradation due to a mean square current amplitude error $\overline{\varepsilon^2}$, namely

$$g_A = g_o \left[1 + \frac{3\pi}{4}\left(\frac{d}{\lambda}\right)^2 \overline{\varepsilon^2}\right]^{-1}$$

where $\overline{\varepsilon^2}$ is the variance of the relative error in current magnitude and d is

Table 6.1 Beamwidth data found by experiment.

Plot	Figure	observed	theoretical	increase
H-plane broadside	6.3	17°	12.8°	33%
E-plane broadside	6.1	17°	12.6°	35%
H-plane ±30° modes	6.4, 6.5	18°	14.7°	22%
E-plane ±30° modes	6.2	15°	14.1°	6.4%
diagonal ±45° modes	6.8, 6.9	20°	17.2°	16%
azimuthal through E-plane 30° mode	6.6	15°	12.8°	17%

the interelement spacing. Although an attempt was made to construct the model network with a final phase error tolerance of ±5°, high humidity and visible corrosion incurred during July, 1981 when most of the testing was done probably raised the standard deviation to around 15° or maybe even higher. A 15° standard deviation would decrease the gain by 6.6% or 0.3 dB, and a 20° standard deviation by 11.5% or 0.5 dB. The amplitude dependence is very slight, for a 25% standard deviation still reduces the gain by only 3.6% or 0.15 dB. The observed degradation in the best scanning mode, the E-plane ±30° beam, was about $1/(1.064 \times 1.17) = 0.803$ or 0.95 dB, so there was probably about 0.3 dB or 0.5 dB gain loss due to mutual effects even in the best case.

The nulls in the pattern show the worst effects when they do not go all the way to the center of the graph. Considering the sum of 8 field vectors, the beam maximum occurs when all are aligned, and with Gaussian phase errors the expected maximum gain is g_ϕ. But the first null occurs when the vector sum is zero and the progressive phase shift produces the octagonal phasor diagram of Figure 6.10a. Likewise the second null is diagrammed in Figure 6.10b. Phase errors are quite visible at the nulls of the field pattern since they cause the ends of the phasors not to meet. The first nulls in the H-plane patterns indicate the worst cases of this.

The slight rippling seen on the main beam of all plots is not due to mechanical flutter of the pen but rather to diffraction from the edges of the range roof. A ray from the antenna striking the sharp edge of the roof is diffracted completely around the edge, the energy leaving in a cone of revolution at the same angle with the edge as the angle of incidence. Some diffracted energy always reaches the probe, adding and canceling coherently as the boom swings in its arc, with the effect of superimposing slight oscillations in the field pattern.

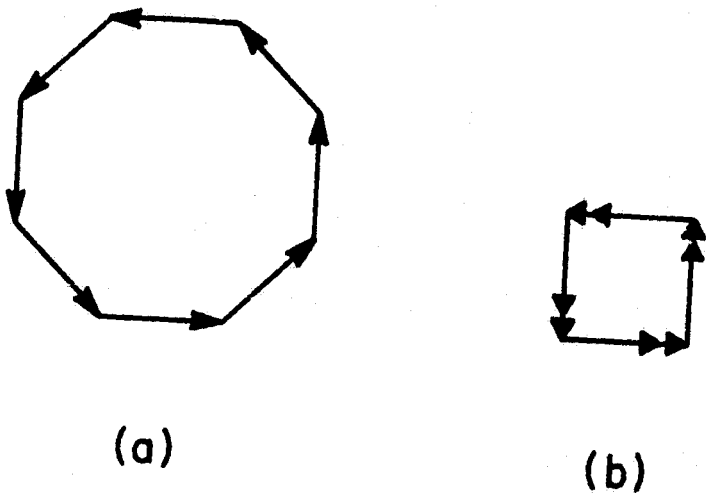

Figure 6.10 First and second nulls for the sum of 8 vectors.

7. CONCLUSIONS AND RECOMMENDATIONS

7.1 Feasibility Projections for Full-Scale Operation

The model array performed as was expected, within the limits of the design. The feed system based on $\lambda/2$ and $\lambda/4$ transformers is a good choice since it can be built to function well in the various scanning modes without the most critical tolerances, this criterion being an absolute necessity in the construction of a large outdoor array which must operate with relatively low maintenance for a decade or more. The E-plane plots of Figures 6.2 and 6.6 showing 6.4% and 17% beamwidth error are indicative of the quality of the model feed system, and a full-scale transmission line network constructed with the techniques related in Allman and Bowhill (1976) should be at least as accurate as the model. Allman also describes a relatively simple procedure with a vector voltmeter for adjusting the phases of individual elements at low power, as long as some slack is left in the lines connected to the pipes.

The worst case of mutual coupling evidently occurred when the two collinear edge rows were completely fed by only two out of the four driven ports (shown in Figure 4.8), thus unbalancing the four input loads. Whether the beam widening was due to the 4-way power splitter or mostly to errors further toward the elements, a less-than 3 dB loss in gain should still be encouraging since input matching would be needed only at the common ports feeding 16 equiphase elements. In a larger array the situation would be expected to improve since there would be more interior elements to balance the loads, and to be pessimistic any coupling effects at the edge should be no worse than in the model since induced voltages are negligible after about 8 rows according to the mutual-impedance computations by Tanner (1982). In other words, to any element more than 8 rows from the edge, the environment

during a particular progressive phase shift looks the same. The elements in each column would be tied together by open-air transforming lines which can be made virtually lossless in order to combat phase errors introduced beyond the matching network. Accurate matching would be easier to achieve at 40.92 MHz than by soldering and taping on microstrip, and even with errors in the model network accepted, no evidence of blind angles could be observed in any of the scanning modes.

7.2 Suggestions for a Full-Scale System

Mayes and Tanner (1981) have proposed a method of power distribution with open-wire lines normal to the array dipoles and shielded coaxial lines parallel to the dipoles, a scheme which provides for the 16 separate ports necessary to scan in any direction mentioned. A similar scheme will be discussed now in more detail. The open-wire lines are tapped every fourth row (2λ) and quarter-wave transformers connect to the element driving points, thus insuring equal currents as required on these elements. Double $\lambda/4$ transformers (see Figure 4.7) may be inserted in these lines periodically to stepup the low impedance caused by a lot of elements in parallel. S. A. Bowhill has lately expressed interest in a hoop arrangement with each conductor pair spread by two concentric circles cut from large diameter PVC pipe, as shown in Figure 7.1. Tanner (1982) discusses the optimum orientation of these lines for coupling considerations. The whole bundle is given a quarter-twist every row in order to bring the tap points on the proper conductor pair directly below the element to be connected. These open-wire lines would in turn be driven by the shielded (to reduce coupling) coaxial lines connected every fourth column. Mayes and Tanner (1981) suggest baluns there so that an unbalanced coaxial line can drive a balanced conductor pair. If an air-dielectric coaxial line is used, the baluns would be 2λ

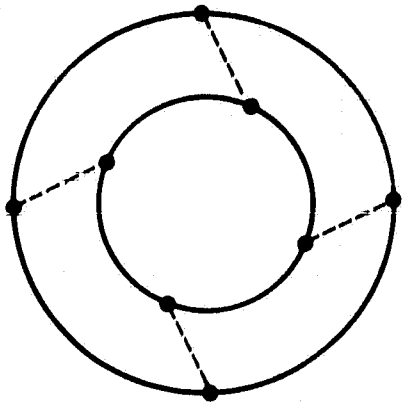

Figure 7.1 Hoop arrangement of open-wire conductors feeding an array column.

apart for equal-voltage connections. An effective 3 λ could be fit to the same distance with most commercial dielectric lines if so desired. There would also be enough room at the connections for a coaxial version of the half-wave balun discussed in Section 4.2. A drawing of a suggested network is shown in the top view Figure 7.2 where a single line along a column indicates each open-wire pair, and a dashed line shows the conductor pair on the underside of the bundle. A dot shows the connection between the open-wire and the element via $\lambda/4$ transformer (not shown); an X signifies a connection on the bottom of the hoop between the open-wire and a coaxial line, shown as a line extending out of the array (the balun is also not shown). A total of 16 coaxial lines can be seen to control element phasing over the entire array for any scan angle required. The original proposal called for a switching and matching network involving four phased sources, but the 180° phase-shift property of a $\lambda/2$ length of line makes a network possible with only two sources that are more evenly loaded.

As shown in Figure 7.2, it is a simple matter to bring all four ports controlling the a-columns to a single point, the lengths extending the same distance $n\lambda/2$ from the nearest array connection (n an integer). Likewise the c-column ports can be brought together about a half-wavelength away, and the b- and d-column ports also brought to about $\lambda/2$ apart. If the ports are physically stacked by A-, B-, C-, and D-rows as shown in Figure 7.3a, the following scheme is possible. Letting a straight line represent a $\lambda/2$ section and a bent line represent a whole λ, the indicated element phases can be realized by the connections shown, with an in-phase source I and a quadriphase source Q. Vertical connections linking the rows are also shown on the sides of the drawings. If the connections from Q are altered by replacing all $\lambda/2$ sections by λ sections and vice versa, the beams listed in

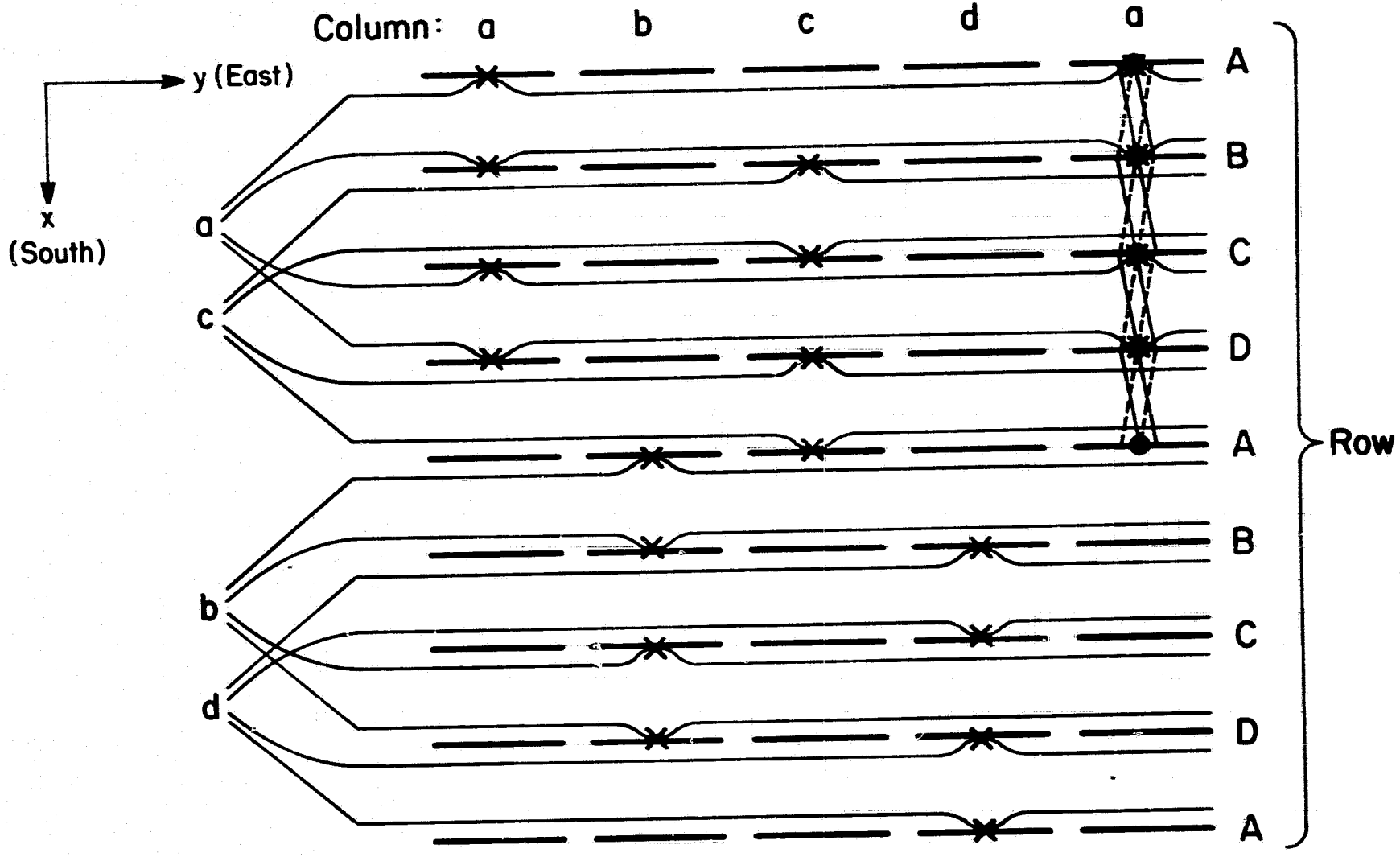

Figure 7.2 Method of feeding array. Dots are open-wire-to-dipole connections, Xs are coaxial-to-open-wire connections from underneath hoops.

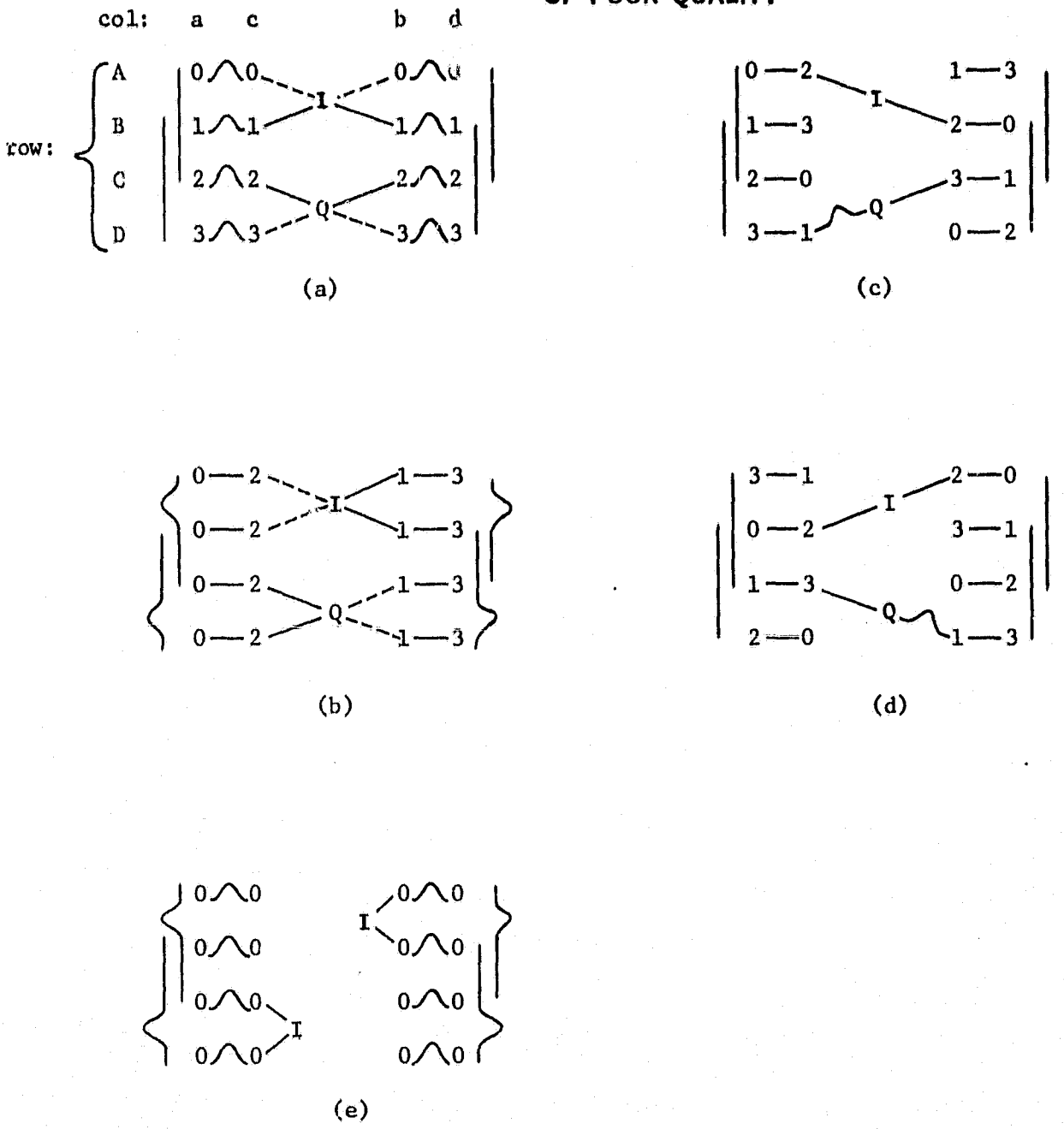

Figure 7.3 Method of connecting ports with λ/2 (straight) and λ (bent) sections for various scanning modes. Source Q leads source I by 90°. Port numbers are multiples of 90° as in Figure 2.1.

(a) H-plane; 30° toward north
(b) E-plane; 30° toward west
(c) $\phi = -135°, +45°$; 45° toward N-W
(d) $\phi = +135°, -45°$; 45° toward N-E
(e) broadside beam

Dashed connections flip the beam to the other side of the vertical.

Figure 7.3 will all appear on the other side of the vertical (the phase progression would be reversed). All of the a- to c- and b- to d- column connections are achieved with only 2 x 2 selections, and since 88 is a multiple of 4 both sources drive the same number of edge-row and edge-column elements in all modes. Some matching may still be required, but some helpful symmetries exist to reduce the magnitude of the problem. In all four diagonal modes available from Figure 7.3c and 7.3d the impedance seen by I never changes, and the same is true for Q. In the E- and H-plane beams of Figure 7.3b and 7.3a, in order to reverse the phase progression one could simply switch to the dashed connections and leave the matching networks after I and Q intact. Any connection possible for the broadside case will load equal impedances onto both sources I. So only four pairs of matching networks would be needed at most, and the two loads of Figure 7.3b may be close enough to the equal loads of 7.3e that one duplicate-pair network may serve all. Mechanical contact switches are certainly feasible and probably the least expensive alternative. For two equal loads matched to lossless lines, the easiest way to split the transmitter power into sources I and Q and introduce a 90° phase shift between them is simply by inserting a $\lambda/4$ extension between I and the duplicate matching network. This may be utilized if the same network is possible between the broadside and the E-plane scan modes. For the others, Π-networks are available from LC network theory when the matching network may as well include the 90° phase shift. For the configuration of Figure 7.4, the design values of the three admittances is given by (Westman, 1956)

$$Y_c = -j\sqrt{Y_1 Y_2}\,\csc(\phi \pm 45°)$$

$$Y_a = -jY_1\cot(\phi \pm 45°) - Y_c$$

$$Y_b = -jY_2\cot(\phi \pm 45°) - Y_c$$

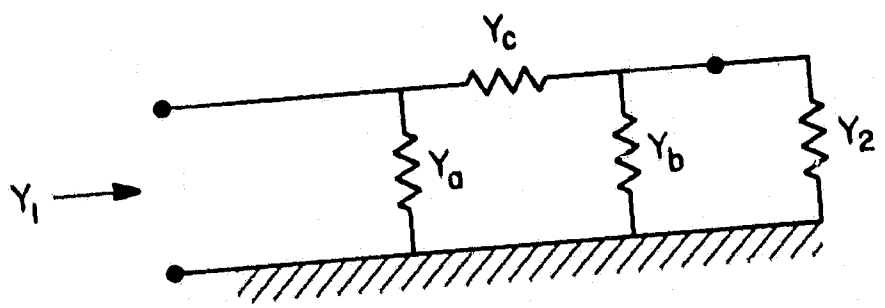

Figure 7.4 Π-network for matched phase shift.

where Y_2 is a function of the scan angle (and mutual effects), $1/Y_1$ should ideally look like 100 Ω, and ϕ is a degree of freedom which may be chosen by the designer. One pair of Π -networks for all diagonal modes, a pair for the H-plane $\pm 30°$ modes, and one other identical pair could then be designed for each load Y_2, assuming that the E-plane mutual effects are sufficiently balanced. At the one main port, the transmit-receive switch design described by Allman and Bowhill (1976) or the prototype currently in operation at the Urbana Radar may be adapted for the new array.

Instead of feeding the whole array from one location, there is the possibility of breaking it down into 4 or 9 subarrays and feeding each separately. This would destroy the overall symmetry inherent in the above matching considerations, though there would still be some symmetry, and the worst that could be encountered is the situation requiring 9 pairs of matching networks for each subarray. For the advantage of being able to operate each subarray separately. the above switching scheme repeated for each subarray would continue to be the simplest yet devised.

REFERENCES

Agrawal, V. D., and Y. T. Lo (1972), Mutual coupling in arrays of randomly spaced antennas, IEEE Trans. Antenna Propagat., AP-20, 288.

Allman, M. E., and S. A. Bowhill (1976), Feed system design for the Urbana incoherent-scatter radar antenna, Aeron. Rep. No. 71, Aeron. Lab., Dep. Elec. Eng., Univ. Ill., Urbana-Champaign.

Buneman, O. (1962), Scattering of radiation by the fluctuation in a non-equilibrium plasma, J. Geophys. Res., 57, 2050.

DeMaw, M. F. (May 1980), RF coaxial cables - choosing the right one, RF Design 3, 12.

Edwards, B., ed. (1981), Research in aeronomy October 1, 1980-March 31,1981, Prog. Rep. No. 81-1, Aeron. Lab., Dep. Elec. Eng., Univ. Ill., Urbana-Champaign.

Evans, J. V. (1969), Theory and practice of ionosphere study by Thomson-scatter radar, Proc. IEEE, 57, 496.

Farley, D. T., J. P. Dougherty, and D. W. Barron (1961), A theory of incoherent scattering of radio waves by a plasma, II: Scattering in a magnetic field, Proc. Roy. Soc. (London), A263, 238.

Gibbs, K. P. and S. A. Bowhill (1979), The Urbana coherent-scatter radar: synthesis and first results, Aeron. Rep. No. 90, Aeron. Lab., Dep. Elec. Eng., Univ. Ill., Urbana-Champaign.

Hammerstad, E. O. (Sept. 1975), Equations for microstrip circuit design, Proc. Europ. Microwave Conf. (Hamburg), 268.

Hansen, R. C., ed. (1966), Microwave Scanning Antennas, Vol. II, Academic Press, New York.

Jasik, H. (1961), Antenna Engineering Handbook, McGraw-Hill, New York.

Jordan, E. C. and K. G. Balmain (1968), Electromagnetic Waves and Radiating Systems, 2nd Ed., Prentice-Hall, Englewood Cliffs, NJ.

Lange, J. et al. (1968), S-parameters... circuit analysis and design, Application Note 95, Hewlett-Packard, Palo Alto.

Lechtreck, L. W. (1968), Effects of coupling accumulation in antenna arrays, IEEE Trans. Antenna Propagat. AP-16, 31.

Lee, S. W. (1977), Uniform asymptotic theory of electromagnetic edge diffraction-a review, Electromag. Lab. Rep. No. 77-1, Electromag. Lab., Dep. Elec. Eng., Univ. Ill., Urbana-Champaign.

Mayes, P. E. (1965), Electromagnetics for Engineers, Edwards Bros., Ann Arbor.

Mayes, P. E. (1981), personal communication, Dep. Elec. Eng., Univ. Ill., Urbana-Champaign.

Mayes, P. E. and D. R. Tanner (1981), Design studies of phased-array for Urbana coherent-scatter radar, Aeron. Lab., Dep. Elec. Eng., Univ. Ill., Urbana-Champaign, unpublished.

Nagle, J. J. (Dec. 1979), Calculations predict bandwidth effects of half-wave balun, Electronic Design, 25, 100.

Przedpelski, A. (June, 1980), Line matching transformers, RF Design, 3, 24.

Rastogi, P. K. and S. A. Bowhill (1976), Scattering of radio waves from the mesosphere-II. Evidence for intermittent mesospheric turbulence, J. Atmos. Terr. Phys., 38, 449.

Rastogi, P. K. and R. F. Woodman (1974), Mesospheric studies using the Jicamarca incoherent-scatter radar, J. Atmos. Terr. Phys., 36, 1217.

Rottger, J. (1981), Investigations of lower and middle atmosphere dynamics with spaced antenna drifts radars, J. Atmos. Terr. Phys., 43, 277.

Ruze, J. (1966), Antenna tolerance theory-a review, Proc. IEEE, 54, 633.

Schelkunoff, S. A. (1952), Advanced Antenna Theory, John Wiley, New York.

Tanner, D. R., Phased array and feed system design in presence of mutual coupling for the proposed Urbana coherent scatter radar antenna, MS thesis, Aeron. Lab., Dep. Elec. Eng., Univ. Ill., Urbana-Champaign.

Weeks, W. L. (1968), Antenna Engineering, McGraw-Hill, New York.

Westman, H. P., ed. (1956), Reference Data for Radio Engineers, I.T. and T., New York.

Wheeler, H. A. (1965), Transmission-line properties of parallel strips separated by a dielectric sheet, IEEE Trans. Microwave Theory Tech., MTT-13 172.

Ziemer, R. E. and W. H. Tranter (1976), Principles of Communications, Houghton Mifflin, Boston.